HT overprint of HP granulites in the Oisans-Pelvoux massif: Implications for the dynamics of the Variscan collision in the external western Alps

Jean-Baptiste Jacob, Emilie Janots, Stéphane Guillot, Daniela Rubatto, Kévin Fréville, Jérémie Melleton, Michel Faure

HT overprint of HP granulites in the Oisans–Pelvoux massif: implications for the dynamics of the Variscan collision in the external Western Alps.

Jacob Jean-Baptiste[1], Janots Emilie[1], Guillot Stéphane[1], Rubatto Daniela[2], Fréville Kévin[3], Melleton Jérémie[4], Faure Michel[5]

[1]Univ. Grenoble Alpes, Univ. Savoie Mont Blanc, CNRS, IRD, univ. Gustave Eifel, ISTerre, 38000 Grenoble, France
[2]University of Bern, Institute of Geological Sciences, Baltzerstrasse 1-3, CH-3012 Bern, Switzerland
[3]UMR 6249 Chrono-environnement, Université de Franche-Comté, Besançon, France
[4]Bureau de Recherches Géologiques et Minières, 3 avenue Claude-Guillemin, BP 36009, 45060 Orléans Cedex 2, France
[5]Institut des Sciences de la Terre d'Orléans, Université d'Orléans, CNRS, 45071 Orléans Cedex 2, France

ABSTRACT

The Oisans–Pelvoux massif belongs to the Paleozoic basement of the External western Alps and records high temperature (HT) metamorphism associated with intense migmatization during the syn to post-collisional stages of the Variscan orogeny. Metamorphic assemblages related to the early collision stages have been obliterated making it difficult to constrain the earlier evolution of the unit. In this study, we report the finding of new bodies of high pressure (HP) mafic granulites, which preserve relics of the prograde evolution. Relics of Mn-rich garnet cores containing inclusions of epidote, titanite, chlorite and rare white micas constrain an early prograde stage at 460–550 °C and 0.4–1.0 GPa. The HP assemblage consists in garnet + clinopyroxene+ quartz + rutile ± plagioclase ± amphibole ± biotite and yield peak-P conditions at 650–730 °C and 1.5–1.7 GPa. Decompression was associated with heating to HT granulite-facies conditions of 800–870°C and 0.6–0.9 GPa, which led to the development of granoblastic polycrystalline mosaics over the resorbing HP assemblage. The U–Pb dating of magmatic zircon cores constrains the emplacement age of the mafic protoliths at 479±5 Ma. Timing of the prograde to HP evolution is estimated around 345–330 Ma based on rutile U-Pb dating, which is contemporaneous with HP recorded in the other crystalline massifs of the western Alps. Zircon metamorphic rims yields U–Pb dates scattering between 337 and 294 Ma, which are interpreted to record crystallization during decompression and heating to granulite facies. Metamorphic conditions during the early prograde stage precludes scenarios involving subduction of a cold passive margin and are better reconciled with thickening of an orogenic wedge during collision. In contrast with other Variscan HP relics of the external Alps, the HP rocks of the Oisans–Pelvoux massif record heating to HT granulitic conditions during decompression, which may result from longer residence time in the lower crust before exhumation.

key words: Variscan HP metamorphism, Petrochronology, Granulites, HT metamorphism

1. INTRODUCTION

High pressure (HP) metabasic rocks have been widely used as a geodynamic marker for subduction. This association mainly arises from the study of active collisional and accretionary orogens, where HP metabasic rocks are found in-context, leaving little ambiguity about their tectonic setting of formation: tectonic accretion in a subduction wedge, subduction of oceanic lithosphere or subduction of continental units containing basic protoliths (Guillot et al., 2008, Lardeaux et al., 2006). Typically, eclogite-facies metabasic rocks are found in association with blueschist-facies metasediments and/or serpentinites in large HP units, which extend over tens to hundreds of kilometers and define suture zones, which correspond to the relics of subducted oceanic or hyperextended lithosphere basins.
In contrast, ancient orogens present a much more complex and ambiguous record, due to erosion of upper structural levels, tectonic overprint during the late collisional stages, and partial re-equilibration of HP metamorphic assemblages at lower P and/or higher T following the HP stage (O'Brien and Rotzler, 2003). By analogy with active orogenic settings, these HP relics have nevertheless been commonly attributed to subduction processes, and have been used to infer the position of the former sutures, despite the lack of clear structural evidences indicative of a suture zone. A typical case of such ambiguous records is the Variscan belt of Europe, which formed during the Devonian and the Carboniferous by collision between Gondwana, Laurussia and a debated number of microplates squeezed in between (Matte, 2001). HP metabasic rocks are widespread in the Variscan belt (Figure 1), but they mostly occur as isolated lenses and boudins in high-grade gneiss and migmatites, which otherwise rarely preserve evidences of an early HP stage. Thus, the geodynamic significance of these isolated HP metabasic rocks remains controversial. They have commonly been interpreted as the relics of one or several Devonian subduction zones, which would mark the suture between the different continental plates involved in the Variscan collision (e.g. Pitra et al., 2021, Benmammar et al., 2020). However, the continuity of these sutures across the orogen remains elusive, due to the scattering of the HP relics over wide areas. Alternatively, it has been proposed that these high-grade – migmatitic – domains containing HP relics are unrelated to subduction, but represent exhumed portions of the orogenic lower crust, which equilibrated at eclogitic or HP granulitic conditions during the Carboniferous collision (e.g. O'Brien and Rötzler, 2003; Whitney et al., 2020). This latter interpretation relies on the fact that most of the HP metabasic rocks record conditions in the HT eclogite of HP granulite facies, and very few were equilibrated along low-T gradients typical of oceanic subduction.

However, this lack of LT-HP rocks may also be a bias due to overprinting of the early metamorphic assemblages during exhumation. Robust thermobarometric and geochronological data are necessary to discriminate between these two models.

.

Rare samples preserving relics of the prograde evolution are therefore invaluable, as they provide key petrographic constraints to understand the geodynamic significance of the Variscan HP metabasic rocks.

We present here new results on the Variscan basement of the external western Alps, in the Oisans–Pelvoux massif. This massif has been recognized as a portion of orogenic middle-to-lower crust, which has undergone HT metamorphism and intense migmatization during the syn to post-collisional stages of the Variscan orogeny. This HT migmatitic stage obliterated most of the pre-HT metamorphic history, and no indisputable evidence of an earlier HP metamorphic stage had been recognized so far in this massif (Grandjean et al., 1996). This metamorphic record strongly contrasts with that of the other basement massifs in the external western Alps, which present several relics of Variscan eclogites and HP granulites (Guillot and Ménot, 2009; Jacob et al., 2021; Jouffray et al., 2020; Paquette et al., 1989; Rubatto et al., 2010), but are comparatively less affected by the HT migmatitic event. As a consequence, the early stages of the Variscan collision remained unconstrained in the Oisans–Pelvoux massif.

Our recent field investigation of high-grade metamorphic domains has identified mafic HP granulite bodies that contain a relict garnet-clinopyroxene HP assemblage overprinted by a HT granulitic assemblage. These granulites are the first documented Variscan HP rocks in the Oisans–Pelvoux massif, and they represent a unique opportunity to constrain the complete metamorphic evolution from collisional to post-collisional stages. The HP granulite bodies were investigated using a multi-method approach, which combined petrologic and microtextural observations, phase equilibrium modeling and Zr-in-rutile thermometry to constrain the P-T evolution, and U-Pb dating of zircon and rutile to constrain the timing of metamorphism. This contribution aims to present the results of these detailed investigations, and discuss the implications for the Variscan geodynamic evolution of the Oisans–Pelvoux massif. In particular, preservation of early prograde stages of the metamorphic

111 evolution provides important constraints regarding the thermal regime of the middle and the lower crust
112 during the early stages of collision.

113 2. GEOLOGICAL SETTING AND FIELD DESCRIPTION

114 2.1. General setting and Variscan evolution

115 The Oisans-Pelvoux massif is located in the French western Alps and belongs to the External
116 Crystalline Massifs (ECM), which form exposed portions of the Variscan basement on the former
117 European margin of the Piemonte-Liguria ocean (Guillot and Ménot, 2009; Von Raumer et al., 2009).
118 This massif has a roughly circular shape of ca. 35km in diameter and exposes high grade metamorphic
119 domains of the Variscan orogenic root (Figure 1). It is mainly composed of early to mid-Paleozoic
120 units, which were metamorphosed and intruded by granitoids during the Variscan orogeny. The
121 basement is caped by non-metamorphic sediments deposited in small pull-apart basins between the late
122 Carboniferous and the early Permian (Fernandez et al., 2002; Guillot and Ménot, 2009). The Alpine
123 collision in the early-mid Eocene (ca. 40 Ma), was responsible for burial and development of
124 greenschist-facies metamorphic assemblages (Bellanger et al., 2015), that are mostly concentrated in
125 Alpine compressional and strike-slip shear zones (Bellahsen et al., 2014; Marquer et al., 2006).
126 The pre-Variscan protoliths derive from a variety of sedimentary and igneous rocks mostly emplaced
127 during the Cambrian–Ordovician period (Fréville et al., 2018; Paquette et al., 1989; Von Raumer et al.,
128 2013). Volcano-sedimentary and bimodal plutonic series of Devonian–Tournaisian age (ca. 370–350
129 Ma, Fréville et al., 2018; Guillot and Ménot, 2009; Ménot, 1987), presumably emplaced in an arc or
130 back-ac setting, are exposed in the western part of the massif (Figure 1). They are strongly affected by
131 Variscan tectono-metamorphic events, and their formation therefore predates the main Variscan
132 collision stages.
133 The Variscan Orogeny in the ECMs occurred from ca. 350 to 295 Ma (Fréville et al., 2018;
134 Guillot and Ménot, 2009). The general tectono-metamorphic evolution is summarized here in three
135 main phases:
136 1. An early Carboniferous (Visean) collisional phase associated with nappe stacking and crustal
137 thickening, which formed E–W vergent nappes, which is associated with burying of the Devonian–
138 Tournaisian series and the development of amphibolite-facies assemblages (garnet ± kyanite ±
139 staurolite) at ca. 600–700 °C and 0.6–0.9 GPa (Fréville, 2016; Fréville et al., 2018; Guillot and Menot,
140 1999). The age of this phase is constrained at ca. 345–330 Ma by U-Pb dating on monazite and Ar-Ar

dating on micas (Fréville et al., 2018). U-Pb dating of zircon and rutile from eclogite relics exposed in northeast Belledonne and in the other ECMs yields the same age (Jacob et al., 2021; Rubatto et al., 2010; Vanardois et al., 2022), and the development of HP assemblages is therefore correlated with this nappe stacking phase.

2. A phase of transpression, associated with the formation of penetrative, steeply dipping fabrics. In the massifs of Belledonne and Grandes-Rousses, these fabrics form a ten-kilometer-wide high-strain corridor marked by dextral shearing, which extends in the other ECM and is thought to represent a crustal-scale dextral shear zone, which was active from ca. 325 Ma (Guillot et al., 2009; Rossi et al., 2009; Simonetti et al., 2018, 2020). In the Oisans–Pelvoux massif, steep metamorphic fabrics rather display sinistral shearing (Fréville, 2016) and may represent antithetic shear zones developed during transpression.

3. Transpression progressively evolved toward transtension during the late Carboniferous (ca. 310–300 Ma), which resulted in the formation of kilometer to ten-kilometer scale half-graben and pull-apart basins (Ballèvre et al., 2018; Fernandez et al., 2002, and references therein).

The older (pre-Carboniferous) metamorphic sequences are intruded by numerous Variscan granitoids, which form about 25% of the exposed area in the Oisans–Pelvoux massif. These granitoids were emplaced from the Visean to the late Carboniferous – early Permian (ca. 345–295 Ma), with two dominant production peaks around 345–330 Ma and 310–295 Ma (Debon and Lemmet, 1999; Fréville, 2016).

2.2. Field description

The investigated area is located in the inner part of the Oisans–Pelvoux massif and mainly exposes high-grade gneiss and amphibolites identified locally as the Lavey series (Le Fort, 1971), which are intruded by Carboniferous granitoids (Figure 1). Early foliation S1 associated with the nappe stacking phase (1) was only observed as relics and is better preserved further west in upper structural levels (Fréville et al., 2018). Two groups of metamorphic foliations have been observed in the investigated area (Figure 2): (i) flat-lying fabrics (S2h), which display shear criteria and mineral lineations consistent with roughly N–S directed flow (Figure 3-a); steeply-dipping fabrics striking N140° to N160° (S2v), which display sinistral shear criteria (Figure 3-b). Development of both fabrics initiated at supra-solidus or HT sub-solidus conditions, as evidenced by the presence of sheared leucosomes and sheared amphibolite boudins (Figure 3-a,b). S2h is affected by kilometer-scale, low amplitude buckling

171 (Figure 2), which probably results from transpression associated with the formation of S2v fabrics
172 (Fréville, 2016).
173 Both felsic and mafic lithologies underwent significant partial melting and display various
174 migmatitic textures ranging from metatexites to diatexites (Figure S1 in the supplements). None of the
175 collected felsic samples preserved any pre-HT assemblage. Cordierite develops sporadically in
176 aluminous metasediments, which testifies to the high temperature of melting, probably associated with
177 biotite-breakdown reactions above 800 °C (Vielzeuf and Holloway, 1988). By contrast, some of the
178 mafic bodies display little evidence of partial melting, and may exceptionally preserve HP granulitic
179 assemblages. HP granulites are extremely rare in the Oisans–Pelvoux massif, since most of them have
180 been partly or completely retrogressed by reaction with anatectic melts or fluids released during
181 crystallization of these melts. A first occurrence of mafic granulite was found by Pecher (1970) in the
182 eastern part of the massif and reported as the Peyre-Arguet granulites (Figure 1), but early HP stages
183 remained controversial and were disregarded (Grandjean et al., 1996; Pecher, 1970). In this study, a
184 newly discovered body of HP mafic granulites was found in La Lavey valley in the central part of the
185 massif (Figure 1). It forms a hectometer-wide body embedded in flat-lying migmatitic S2h (Figure 3-c).
186 The Peyre-Arguet body lies in a N150° oriented mylonitic shear zone (S2v), and shows more intense
187 overprinting by amphibolite-facies assemblages than the Lavey granulites. The mafic granulite in the
188 Lavey body shows variable degrees of retrogression and deformation (Figure 3-d-e). Some portions are
189 composed of massive, weakly to non-foliated HP mafic granulites (Figure 3-d), whereas others portions
190 present a layered texture parallel to S2h, with alternating centimetric to metric layers of granulites and
191 garnet-free amphibolites (Figure 3-e). The plagioclase-amphibole rich layers generally display a
192 mylonitic texture, while the garnet-bearing layers are much less deformed.

193 # 3. METHODS

194 ## 3.1. Analytical methods

195 Backscattered electron images were acquired at ISTerre Grenoble with a Tescan Vega 3 scanning
196 electron microscope operated with an accelerating voltage of 16 kV and a beam current of 10 nA.
197 Mineral compositions were measured using a JEOL JXA-8230 electron microprobe at ISTerre
198 Grenoble. Garnet analyses were performed with a 15 kV accelerating voltage, a 20 nA beam current
199 and a counting times of 60s for the peak and 30s for the background. The other silicates were analyzed
200 with a 15 kV accelerating voltage, a 10 nA beam current and counting times of 30s for the peak and 15s

for the background. The spot size was set to 1-3 µm depending on the size of minerals and the presence of volatile elements. X-ray element maps were acquired with a 15 kV accelerating voltage, a 100 nA beam current and a 100 ms counting time per pixel. Natural minerals and synthetic glass were used for standardization, and the ZAF matrix procedure was applied for data reduction. X-ray maps were processed using the XmapTools software (Lanari et al., 2014, 2018).

Zr and other trace elements (Nb, Fe, Cr) in rutile were measured in thin section on four samples (JB-19-16; JB-19-18; JB-19-43; JB-19-55), with the JEOL JXA-8230 electron microprobe at ISTerre Grenoble. The instrument was operated with an accelerating voltage of 20 kV, a beam current of 600 nA, and a total counting time of 600s, with spot size set to 1-3 µm. Standardization was done on synthetic and natural standards of TiO_2 ZrO_2, Cr_2O_3, Fe_2O_3 and Nb. The detection limit is around 27 ppm for Zr and below 35 ppm for other trace elements. Accuracy check was done on standard rutile R632 (Axelsson et al., 2018), which returned Zr concentrations between 2 and 5% of the reference value. This uncertainty is consistent with counting error statistics returned by the JEOL microprobe software for rutile analysis, which gives a 2σ uncertainty between 40 and 50 ppm. In addition, rutile grains separated from sample JB-19-56 were analyzed for trace elements by LA-ICPMS at the University of Bern, and were subsequently dated (see below).

Zircon and rutile were separated using conventional rock crushing and heavy liquids. Crystals were mounted in epoxy resin and polished to expose the grain center for analysis. Charge contrast (CC) images of zircon grains were obtained with a ZEISS EV050 scanning electron microscope at the Institute of Geological Sciences, University of Bern, at low vacuum conditions (18 Pa), 12 kV, a beam current of 100 mA and a working distance of 9.5 mm. It has been previously demonstrated that CC images correlate exactly to cathodoluminescence (Watt et al., 2000). Backscatterred electron images of separated rutile grains were obtained at ISTerre Grenoble using the same instrument and analytical conditions as described above.

Trace element spot analysis of separated zircon and rutile was performed with a RESOlution Laser System coupled to an Agilent 7900 quadrupole ICP-MS at the Institute of Geological Sciences (University of Bern). A He-H_2 gas mixture was used as the aerosol transport gas. The laser spot diameter was 24 and 20 µm for zircon, and 38 µm for rutile. The laser was set to 5 Hz repetition rate and an energy density on the sample of 4 J/cm^2. Oxide interferences were reduced by maintaining ThO/Th < 0.2. Sample analyses were calibrated using NIST SRM 612 (Jochum et al., 2011). Accuracy was monitored using the reference material GSD-1G (Jochum et al., 2005) and zircon 91500

(Wiedenbeck et al., 2004), and was assessed to be better than 10% for all elements. Data reduction was performed using the software Iolite (Paton et al., 2011).

U-Pb dating of rutile was performed with the same LA-ICP-MS system at the University of Bern with conditions of 5 Hz and 3.5 J/cm^2. The count rate ratio for Th/U was 98-97 and the ThO/Th < 0.2. Measurements consisted of 30s background and 30s signal acquisition sweeping through the masses ^{206}Pb, ^{207}Pb, ^{208}Pb, ^{232}Th and ^{238}U. Spot size was 50µm with a pre-cleaning with a 60µm beam. U-Pb ratios were standardized to rutile R10 (1091.6±3.5 Ma, Luvizotto et al., 2009), whereas secondary reference material was rutile R632 (496±2 Ma, Axelsson et al., 2018), which returned an average ^{206}Pb/^{238}U of 496±11 Ma. Data reduction was performed using the software Iolite (Paton et al., 2011) running the DRS VizualAge_UcomPbine (Chew et al., 2014), although no common Pb correction was applied to the data of either standards or unknown. The single spot 2σ standard error external on the primary standard was 7.5% and propagated in full to the unknowns.

U-Pb geochronology of zircon was carried out with the SwissSIMS Cameca IMS 1280-HR at Université de Lausanne, which is equipped with an high-brightness Hyperion H201 RF plasma oxygen ion source. Basic instrument set up parameters were 6-8 nA, 20 µm O_2- primary beam, mass resolution M/ΔM ~ 5000, energy window = 40 eV. Data were acquired in mono-collection, peak-hopping mode. U-Pb-Th data were standardized to TEM2 zircon (417 Ma, Black et al., 2003) and accuracy was checked with zircon standard Plešovice (337.17±0.37 Ma, Sláma et al., 2008), which were cast in the same epoxy mount as the unknowns and returned an age at 337.7±3.5 Ma. The uncertainty on standard ^{206}Pb/^{238}U – UO_2/U calibration was 1.0 and was propagated to the data. Common Pb correction was based on the measured ^{204}Pb signal (when significant relative to background) assuming the present-day model terrestrial Pb composition of Stacey and Kramers (1975). Radiogenic ratios and single ages were calculated using the CIPS program compiled by Martin Whitehouse. Age calculations use the decay constant recommendations of Steiger and Jäger (1977). The IsoplotR package (Vermeesch, 2018) was employed to plot the diagrams and calculate concordia and weighted average ages. Individual uncertainties are quoted at 1σ level and the confidence level for weighted average is 95%.

Whole rock geochemical analyses were performed at the SARM in Nancy, using a Thermo Fischer iCap6500 ICP-OES for major oxides and an iCapQ ICP-MS for minor and trace elements. Details about the analytical procedures for whole rock geochemical analyses are described in Carignan et al. (2001). In addition, FeO was measured by wet titration in sample JB-19-43 in order to constrain the Fe^{3+}/Fe^{2+} balance in the mafic granulites.

3.2. Thermobarometry

Zr-in-rutile temperatures for five samples were calculated using the calibration of Kohn (2020), constrained with combined experimental and natural datasets. Two samples of garnet-bearing mafic granulites (JB-19-43 and JB-19-56) were selected for comprehensive P-T estimations using a combination of forward phase equilibrium modeling with PerpleX 6.9.0 (Connolly, 2009) and inverse thermobarometry on plagioclase-amphibole pairs using the edenite-richterite exchange thermometer of Holland and Blundy (1994). Phase equilibrium models were computed in the compositional space MnNCKFMASHTO, using the TC-DS622 thermodynamic database of Thermocalc (Holland and Powell, 2011), with a set of solution models from Fuhrman and Lindsley (1988), Green et al. (2007, 2016), Holland and Powell (1998,2011) and White et al. (2000, 2014). Reactive bulk compositions used as input in PerpleX were obtained by re-integration of Xray maps using XmapTools 3.4.0 and by ICP-OES whole rock analyses. Fe^{3+} inferred by difference between ICP-OES and wet titration measurements in sample JB-19-43 was taken as a maximum value, and was then adjusted iteratively using the *meemum* function of PerpleX, by modifying incrementally the amount of O_2 until a good fit is obtained regarding Fe^{3+}/Fe_{tot} ratios in garnet and clinopyroxene. No evidence of C-S-bearing volatile species have been observed, so fluid was considered as pure H_2O ($a_{H2O}^{Fluid} = 1$). A summary table of input parameters and solution models used to compute each phase diagram is given in Table S1 the online supplements.

P-T conditions of equilibration for the different mineral assemblages were assessed by comparing predicted stable assemblages with petrographic observations, and by plotting selected mineral isopleths. In addition, we used the approach described in Duesterhoeft and Lanari (2020), which allows a more rigorous assessment of the match between predicted and measured mineral composition than the standard isopleth approach. It relies on a set of quality factors, which are computed over the whole P-T grid and take values between 0 and 1, 0 meaning very poor fit and 1 meaning that predicted and measured composition are indistinguishable within uncertainty.

4. PETROGRAPHY AND MINERAL COMPOSITION

Two samples of mafic HP granulite (JB-19-43 and JB-19-56) have been collected in a massive, weakly to non-foliated domain of the Lavey granulite. Another sample (JB-19-55) was collected in a ca. 50 cm thick highly strained layer retrogressed to amphibolite-facies conditions (Figure 3-c). In addition, two mafic granulite samples (JB-19-16 and JB-19-18) were collected in the Peyre-Arguet granulite body,

but they are generally more retrogressed and do not preserve the early prograde and HP stages. The well-preserved HP granulite samples from La Lavey have been used to constrain the P-T evolution, and mineral assemblage and compositional zoning have been investigated in detail. The granulites from Peyre-Arguet are described more briefly. Summary of sample locations and main petrographic features is provided in Table 1. A set of microphotographies of the main petrographic features is shown in Figure 4, and X-Ray maps and composition diagrams and profiles are shown in Figures 5 and 6. The complete set of mineral analyses with additional plots are provided in the supplements.

4.1. La Lavey mafic HP granulites (JB-19-43; JB-19-56)

The two HP granulite samples present very similar mineral assemblages and nearly the same bulk rock composition. Mineral compositions are thus very close, and composition ranges reported below apply for both samples. They contain garnet, clinopyroxene, plagioclase, calcic amphibole, quartz and biotite, with accessory rutile, apatite, ilmenite and zircon (Figure 4-a,b). Garnet in both samples contain inclusions of quartz and rutile. In addition, garnet of sample JB-19-43 contains inclusions of epidote, chlorite, titanite, amphibole and plagioclase. Rare inclusions of white mica, which do not present evidence of phengite substitution, have also been observed in garnet. Epidote, chlorite and titanite are absent in the matrix.

Garnet forms 0.5–3 mm wide grains, which are variably resorbed. The most common resorption texture consists in replacement by granoblastic polycrystalline coronas rich in plagioclase (Figures 4-b and 5-b). Kelyphite with plagioclase + amphibole also occur in sample JB-19-43. Selected grains were imaged by X-Ray mapping in both samples, and compositional variations were quantitatively assessed on 1D profiles (Figure 5). In both samples, garnet displays complex internal zoning. The large garnet grain in sample JB-19-43 is considered to preserve prograde zoning, possibly affected by later diffusion (Figure 5-a). Two domains are distinguished: a Ca-Mn-rich core (Grt-1: $Alm_{48\text{-}49}Prp_{14\text{-}16}Grs_{29\text{-}32}Sps_{04\text{-}08}$) and a Mg-rich rim (Grt-2: $Alm_{49}Prp_{25}Grs_{25}Sps_{01}$), The boundary between Grt-1 and Grt-2 has been blurred by post-growth diffusion and lies in a broad transitional zone, where Ca-Mg-Mn compositions change progressively and are decorrelated from each other. Within Grt-1, there is a gradual concentric increase in Ca and Mg correlated with a decrease in Fe and Mn. Concentric oscillations in Ca observed within Grt-1 are interpreted to result from growth-related processes.

Garnet grains in sample JB-19-56 are smaller and more resorbed than in sample JB-19-43 (Figure 5-b). They display a broad Ca-rich core domain (Grt-1: $Alm_{45-47}Prp_{24}Grs_{28-30}Sps_{01}$) surrounded by a Mg-richer and Ca-poorer domain (Grt-2: $Alm_{49}Prp_{26}Grs_{24}Sps_{01}$). Grt-1 displays patchy Ca-zoning, which may be relics of an initial concentric zoning as observed in sample JB-19-43. Grt-1 and Grt-2 are surrounded by a thin Fe-Mn-richer domain (Grt-3: $Alm_{52}Prp_{25}Grs_{21}Sps_{02}$), which has no equivalent in sample JB-19-43.

Clinopyroxene is a Na-poor augite (Na < 0.03, Ca = 0.85–0.90 per formula unit (p.f.u), Mg# = 0.66–0.76, Figure 6). It crystallizes in symplectites of plagioclase + clinopyroxene, which replaced an earlier generation of coarse-grained Na-richer clinopyroxene, that is however not preserved. An estimate of the composition of primary coarse-grains clinopyroxene has been obtained by re-integrating the composition over a ca. 400 µm-wide symplectite domain in sample JB-19-56 (Figure 6-a). The obtained mineral formula normalized to 6 oxygens is consistent with clinopyroxene (Si = 1.97 p.fu, sum of cations = 3.93 p.f.u) containing 20 ± 3% jadeite (Figure 6-c). *Orthopyroxene* is an enstatite (Mg# = 0.50–0.60) with an Al content between 0.02–0.05 p.f.u. It forms anhedral to sub-euhedral 100–500 µm large grains, and also occurs in small proportions in the symplectites.

Plagioclase mainly crystallizes as fine-grained granoblastic polycrystalline coronas around resorbed garnet (Figures 3-a,b and Figure 6-b). Smaller amount of plagioclase is also found in symplectites with clinopyroxene, which have grown by breakdown of primary coarse-grained clinopyroxene. Plagioclase composition present a large scattering from Na-rich ($An_{18}Ab_{79}Or_{03}$ for the Na-richest grains) to Ca-rich ($An_{48}Ab_{51}Or_{01}$ for the Ca-richest grains) composition. Na-rich plagioclase is found in the core of the grains in the granoblastic domains as well as in the symplectites, while Ca-rich plagioclase is restricted to thin coronas around garnet and at grain boundaries (Figure 6-b,c).

Calcic amphibole is a magnesian and slighlty titanian hastingsite ($Al^{(iv)}$ = 1.5–1.9 p.f.u, Mg# = 0.55–0.67, Ti = 0.16–0.27 p.f.u, $Fe^{3+}/Fe^{3+}+Al^{(vi)} > 0.5$). It forms sub-millimetric euhedral to sub-euhedral prismatic grains, which crystallize around garnet or associated with plagioclase in thin kelyphites in sample JB-19-43. Compositional variations are related to textural position (Figure S7 in the supplements): amphibole in contact with Na-rich plagioclase is poorer in Al ($Al^{(iv)}$= 1.5–1.7) than amphibole in contact with Ca-rich plagioclase ($Al^{(iv)}$ = 1.8–1.9).

Biotite has Mg# between 0.48 and 0.57 and contains about 0.17–0.27 p.f.u Ti. It forms thin 100–200 µm long rods and coarser flakes (up to 1 millimeter-long), which are frequently grouped in

patches associated with amphibole and plagioclase around garnet (Figure 4-b. *Quartz* occurs as small (10–20 µm) inclusions in garnet and also forms larger grains (100–500 µm) in the matrix (Figure 5).

Rutile and *ilmenite* occur in both samples. Ilmenite is the main Ti-bearing phase and forms 100–500 µm long grains, mainly located outside of garnet (Figure 4-a,b and Figure 5). Rutile is mainly preserved as inclusions in garnet, where it forms grains up to 100 µm long, which occasionally display partial replacement by ilmenite and/or contain ilmenite exsolutions (Figure 6-c and Figure 7-a)-. In sample JB-19-43 small (generally < 50 µm) grains of rutile also occur outside of garnet, either in inclusion in amphibole or within the symplectites (Figure 7-b). No rutile was observed outside of garnet in sample JB-19-56. *Zircon* is ubiquitous in the mafic granulites, and occurs either as inclusions in garnet porphyroclasts or in the matrix.

4.2. La Lavey garnet-free amphibolite (JB-19-55)

In contrast with the HP granulites, garnet-free sample JB-19-55 is strongly deformed, with alternating millimeter-thick layers of calcic amphibole and sericitized feldspar. It contains 1–5 mm wide patches composed of a mosaic of equant, fine-grained (<100 µm) euhedral to sub-euhedral clinopyroxene and plagioclase, which are mainly concentrated in the amphibole-rich layers (Figure 4-d). Clinopyroxene is a diopside (Ca = 0.9–0.95 p.f.u, Mg# = 0.75–0.80). Plagioclase composition ranges between An_{39-52}, with no significant difference between the larger sericitized grains in leucocratic layers and the plagioclase + clinopyroxene mosaics (Figure 6-c). Amphibole is mainly a Ti-poor pargasititic hornblende ($Al^{(iv)}$ = 1.41–1.66, Mg# = 0.63–0.68, Ti = 0.12–0.17p.f.u). A few grains of actinolite are also found ($Al^{(iv)}$= 0.30–0.75, Mg# = 0.71–0.75, Ti = 0.02–0.06 p.f.u). Ilmenite is the dominant Ti phase and forms 100–500 µm grains, which are partly resorbed and commonly surrounded by titanite coronas. Rutile is rare and forms small grains (<50 µm), that are commonly rimmed by titanite (Figure 7-c). Tiny grains (5–20 µm) of late rutile (Rt-II) also crystallize in association with titanite over ilmenite (Figure 7-f).

4.3. Peyre-Arguet mafic retrogressed granulites (JB-19-16; JB-19-18)

Sample JB-19-16 is mainly composed of calcic amphibole, garnet, plagioclase, quartz, clinopyroxene relics and accessory rutile, ilmenite, and zircon (Figure 4-e). No orthopyroxene has been observed. Garnet grains are 0.5-2 mm in diameter, partly resorbed and surrounded by a corona of sericitized

plagioclase (Figure 4-e). Clinopyroxene occurs in coarse-grained symplectites, which locally display recrystallization textures in mosaics. In this sample, rutile is only preserved in garnet where it forms up to 200 µm-large inclusions (Figure 7-e).

Sample JB-19-18 contains the same mineral assemblage as sample JB-19-16, except that it completely lacks of garnet, which has been entirely resorbed. It is mainly composed of a granoblastic amphibole and sericitized plagioclase (Figure 4-f), with relics of coarse-grained symplectites of clinopyroxene + plagioclase. Ilmenite is the dominant Ti-bearing phase, but rare, small grains of rutile (<50 µm) are found in inclusion in feldspar and amphibole, or in the plagioclase + clinopyroxene symplectites (Figure 7-f).

5. BULK ROCK GEOCHEMISTRY

Whole rock major and trace element compositions (Table S3 and Figure 8) were obtained on the three samples from La Lavey (JB-19-43,55,56) and on one sample from the Peyre-Arguet body (JB-19-16). All samples except sample JB-19-55 display major element composition of Fe-Ti-rich tholeiitic basalts (Na_2O+K_2O = 3–4 wt%, SiO_2 = 48–50 wt%, TiO_2= 1.9–2.3 wt%, molar $Mg/(Mg+Fe^{2+})$ = 0.39–0.44). Trace element patterns normalized to N-MORB indicate significant enrichment in LREE and other incompatible elements $(La/Yb)_N$ = 3.34–4.26, $(Th/Yb)_N$ = 2.58-7.09). Enrichment is particularly pronounced for elements that are highly mobile in fluids (Cs, Rb, U, Pb), especially in sample JB-19-16, which presents strong spikes in Pb, U and Cs. There is no significant Eu anomaly ($(Eu/Eu^*)_N$ = 0.98–1.04, where $(Eu/Eu^*)_N = Eu_N/(Sm_N.Gd_N)^{1/2}$) and the Nb–Ta anomaly is weak ($(Th/Nb)_N$ = 1.15-1.92). Sample JB-19-55 has a distinct composition both in major and trace elements. It is much richer in K_2O, Al_2O_3 and MgO (Mg# = 0.56) than other samples. The LREE/HREE fractionation is comparable to that of other samples ($(La/Yb)_N$ = 2.56), but REE concentrations are one order of magnitude lower than in other mafic granulites. It presents extreme enrichment in fluid-mobile elements, in particular Cs, Rb, Ba and Pb, it has positive anomalies in Eu ($(Eu/Eu^*)_N$ = 1.74), Sr and Ti, as well as negative anomalies in Nb and Ta ($(Th/Nb)_N$=3.58). The overall low REE, the strong positive anomalies in Eu, Sr and Pb suggest a plagioclase-rich cumulates as protolith. The high K_2O content and the strong enrichment in fluid-mobile elements in this sample suggest pervasive interaction with crustal fluids during metamorphism.

6. THERMOBAROMETRY

6.1. Inverse thermobarometry and forward thermodynamic modeling

The P-T-t evolution of the Lavey granulitic body has been inferred using the three samples JB-19-43, JB-19-56 and JB-19-55. These samples preserve different stages of the P-T evolution and were therefore used to constrain different portions of the P-T path.

- sample JB-19-43 contains garnet with the most complete zoning, and preserved evidence of an early prograde phase characterized by the formation of Mn-rich garnet cores containing inclusions of epidote, chlorite, titanite and rare white mica. It has therefore been used to constrain the early prograde evolution.

- sample JB-19-56 has been used to constrain peak-P / post peak-P decompression at HT based on quantitative X-Ray mapping.

- sample JB-19-55 is heavily retrogressed in amphibolite facies and has been used to constrain retrogression to lower T using inverse thermobarometry.

P-T phase diagrams and mineral composition contours used to constrain P-T conditions are reported on Figure 9. Results of amphibole-plagioclase thermometry are reported on Table 2.

Inclusions of OH-bearing minerals in garnet of sample JB-19-43 indicate that garnet growth initiated under H_2O-rich conditions. This is further supported by the Mn-rich composition of the garnet cores, which could only be reproduced in PerpleX by adding a high amount of H_2O close to fluid-saturation in the reactive bulk (Figure S4 in the supplements). The P-T phase diagram for sample JB-19-43 was therefore computed using the bulk rock composition measured by ICP-OES and assuming saturation in H_2O (Figure 9-a). Garnet becomes stable at ca. 0.4–0.6 GPa, and the combined presence of chlorite, epidote, titanite and white mica indicates equilibration at T between 460 and 550 °C and P between 0.4 and 1.0 GPa (stage 1). The presence of rutile and amphibole inclusions in the garnet core and mantle mark a progressive increase in P and T over 550 °C and 0.8 GPa. This relatively mild T is in line with the preservation of the Ca-Mn-rich garnet core (Grt-1). Ca–Mn isopleths indicate P–T conditions around 550–600°C and 0.8–1.1 GPa for Grt-1. Smoothing of the initial garnet zoning on X-Ray maps indicate post-growth diffusion, particularly for Mg. Therefore, it is likely that garnet composition was partially reset by diffusion exchange and thus the P–T condition estimated for the Mn-rich core is taken as maximal estimate. Increase in Mg-content between Grt-1 and Grt-2 is consistent

438 with increasing T and P during prograde to peak-P evolution, but any quantitative estimate is hampered
439 by post-growth diffusion and fractionation of components in the garnet core.
440 The HP stage (stage 2) has been constrained using a local composition extracted from the X-
441 Ray map in sample JB-19-56. H_2O was treated as a standard thermodynamic component with a fixed
442 amount, which was adjusted to fit with the observed proportion of OH-bearing phases (biotite and
443 amphibole) in the local domain. The mineral mode match criterion (Q_{vol}) of Duesterhoeft and Lanari
444 (2020) indicates reasonably good fit between observed an predicted modal composition (Q_{vol} >80%)
445 over a wide domain between 0.5 and 1.5 GPa (Figure S-6 in the supplements). The local composition
446 used in input is therefore considered to be appropriate within this range. The HP stage assemblage
447 (stage 2) is inferred as Grt-2–Cpx–Qtz–Rt, possibly with plagioclase, amphibole and/or biotite.
448 Although Na-rich clinopyroxene is no longer present, its composition was inferred from compositional
449 mapping through the symplectites, indicating a reintegrated composition of ca. 20% Jd. Phase diagrams
450 computed for samples JB-19-56 and JB-19-43 (Figure 9) both predict presence of OH-bearing
451 minerals, either amphibole + biotite or phengite, up to HT conditions. Some inclusions of amphibole
452 are present in garnet of sample JB-19-43 and thus, it is likely that amphibole, and possibly biotite were
453 part of the peak-P assemblage. The stability field of the HP assemblage corresponds to a broad domain
454 between 600–800°C and 1.0–1.8 GPa (Figure 9-b). Composition quality factors (Q_{cmp}) computed for
455 Grt-2 yields the best match at 650–730°C and 1.5–1.7 GPa. This P–T range is consistent with the
456 jadeite content in clinopyroxene estimated by re-integration, which constrains P around 1.55–1.65 GPa
457 for the same range of T.
458 Two HT decompression stages (stages 3 and 4) are distinguished from mineral zoning and
459 assemblages in JB-19-56. Decompression is associated with resorption of garnet and clinopyroxene,
460 which breakdown into plagioclase, Na-poor clinopyroxene, amphibole, and then orthopyroxene below
461 ca. 1.0 GPa. Biotite and quartz are also part of this assemblage. Most of the plagioclase in the
462 symplectites and the granoblastic coronas around resorbed garnet is Na-rich (An_{18-30}), which according
463 to our thermodynamic calculations indicates that most of the resorption occurred at relatively high-P
464 between 1.0 and 1.3 GPa (Figure 9-c). Temperature during this first stage of decompression (stage 3)
465 was likely relatively high, as evidenced by relatively K-rich plagioclase cores (Or_{03}), which indicates T
466 around 750–800 °C, and high Ti-content in biotite (> 0.2 p.f.u), which implies equilibration between
467 780 and 820 °C. These temperatures are consistent with those estimated by inverse thermobarometry
468 on Na-rich plagioclase – Al-poor amphibole pairs, which yield an average T = 764 ± 27 °C (assuming P

= 1.2 GPa), both in the granoblastic coronas and in the symplectites. The formation of the thin Ca-rich plagioclase rims around garnet and at grain boundaries (An_{40-48}) indicates a second stage of decompression to 0.6–0.9 GPa (stage 4). This stage is associated with the formation of the thin garnet rims (Grt-3) in sample JB-19-56, which presents an increase in Mn relative to Grt-2, and can only be reconciled with growth at low-P close to the Grt-out boundary. Q_{cmp} computed for Grt-3 yields a good fit between 0.7 and 1.0 GPa and over a wide range of T (650–900°C). The edenite-richterite thermometer applied to Al-rich amphibole in contact with Ca-rich plagioclase yields high T at 833±34 °C (assuming P = 0.8 GPa). Thus, sample JB-19-56 records decompression from HP conditions at 650–730 °C and 1.5–1.7 GPa to 0.7–1.0 GPa and 800–870°C, which corresponds to an increase in T of ca. 100–200 °C during decompression.

Sample JB-19-55 is heavily retrogressed in amphibolite facies (stage 5). We used plagioclase-amphibole pairs located at the interface between amphibole and plagioclase-rich layers to constrain T. These minerals presumably crystallized during retrogression at lower P than the HT stage 4, and therefore temperature estimates are reported for an assumed pressure of 0.4 GPa. Pargasitic hornblende – plagioclase pairs yield an average T at 656±34 °C (13 pairs), while actinolite – plagioclase pairs yield an average T at 573±44 °C.

In contrast with the Lavey HP granulites, the Peyre-Arguet granulite is more retrogressed, and samples JB-19-16 and JB-19-18 are less suitable to determine P-T path, particularly for the prograde or HP stages. Given the presence of retrograde textures similar to that of the Lavey samples (e.g. plagioclase corona around garnet in JB-19-16, and conspicuous clinopyroxene–plagioclase symplectite relics), the Peyre-Arguet samples possibly underwent a HP stage followed by HT decompression. This HT metamorphism is independently confirmed by the Zr-in rutile thermometry (see below).

6.2. Zr-in-rutile thermometry

Rutile was analyzed in different textural settings in the five samples from La Lavey and Peyre-Arguet. Several grains were analyzed in multiple spots to check possible core-rim zoning. Variation in Zr-content within a single grain are generally small to insignificant, ruling out significant loss of Zr by diffusion in the rims.

Several populations of rutile are distinguished based on textural position and Nb-Zr systematics (Figure 10a). Rutile inclusions in garnet generally display low Nb content (<1000 ppm, except a few grain in sample JB-19-43 with higher Nb) and large scattering in Zr (304–1119 ppm in

sample JB-19-43 and 355–1298 ppm in sample JB-19-16). In sample JB-19-43, highest Zr-contents are observed in rutile inclusions that are partially replaced by ilmenite. Rutile grains that are located close to or in contact with zircon do not display any significant difference in Zr content.

In contrast, matrix grains display important scattering in Nb (470–2350 ppm in sample JB-19-43, 180–2310 ppm in sample JB-19-55 and 800–3750 ppm in sample JB-19-18), and high Zr content (851–1291 ppm in sample JB-19-43, 803–1223 ppm in sample JB-19-55 and 1147–1593 ppm in sample JB-19-18). Rutile grains separated from sample JB-19-56 and analyzed by LA-ICPMS are devoid of ilmenite replacement / exsolution and form a cluster of Nb-Zr poor analyses (Nb = 500–890 ppm, Zr = 220–342– ppm) similar to those of rutile inclusions in garnet. No matrix rutile was observed in the petrographic thin section of sample JB-19-56, and therefore it is very likely that the separated grains were initially included in garnet. Finally, late rutile found around ilmenite in sample JB-19-55 displays very low Zr and Nb content (Nb = 28–124 ppm and Zr = 41–78 ppm).

Temperatures were obtained using the calibration of Kohn (2020) , which has a dependence in P of ca. +50°C.GPa^{-1}. According to phase diagrams computed for samples JB-19-43 and JB-19-56, rutile may have equilibrated anywhere between 0.8 and 1.6 GPa during the prograde or the retrograde evolution. A value of 1.2 GPa was thus used for all the grains, except for the late rutile in sample JB-19-55, which is assumed to have formed during late retrogression and for which P was set to 0.4 GPa. Applying a nominal P of 1.2 GPa yields to slightly underestimate or overestimate the T if the rutile formed respectively at higher or lower P. Considering the possible range of P for rutile growth, this uncertainty is at most ±20 °C. There are no P estimates for rutile of the Peyre-Arguet samples, but considering the strong similarities in mineral assemblages with the samples from La Lavey, these rocks may have evolved approximately within the same range of P. Therefore, uncertainties related to unknown P during rutile growth are within the same range of ±20°C.

Quartz is stable over the whole stability field of rutile (Figure 9) and zircon seems to have been reactive over a large part of the P–T evolution, as suggested by the large range of U–Pb dates in metamorphic zircon rims (see below). We therefore assume that rutile has grown under SiO_2 and ZrO_2 saturated conditions.

The separated grains of rutile (JB-19-56) consistently yield low T between 611 °C and 650 °C (Figure 10b). The large spread of Zr content in rutile inclusions (samples JB-19-43 and JB-19-16) translates into a spread in temperature from 637 to 775 °C in sample JB-19-43 and from 654 to 793 °C in sample JB-19-16. In contrast, matrix rutile yields T clustered between 743 °C and 792 °C in sample

JB-19-43, between 737 and 785 °C in sample JB-19-55 and between 778 and 818°C in sample JB-19-18. Finally, low-Zr rutile in sample JB-19-55 yields low T between 457 and 499°C, although with large uncertainty (ca. 40–60 °C), due to the poor precision on the Zr measurements.

7. U-Pb GEOCHRONOLOGY

7.1. Composition and internal textures of zircon and rutile

The garnet-bearing mafic HP granulite JB-19-56 was selected for U-Pb dating of zircon and rutile. Zircon grains are typically 100–200 µm in size and are rounded to sub-euhedral (Figure 11-a). They present CC-dark cores with common oscillatory or broad sector zoning. Most of the zircon cores show homogeneous CC-bright rims of variable width (10–50 µm), which display embayments. Rutile grains separated for U-Pb dating are 100-250 µm in diameter and are completely devoid of ilmenite exsolutions or replacement.

Thorium and U content in zircon were measured during SIMS analysis and values are generally consistent with LA-ICPMS data measured on the same domain, considering the different volumes sampled. LA-ICPMS trace element analyses of zircon grains were filtered by monitoring P, Y, Sr, Ti and Nb, and analyses presenting an unusually high concentration of these elements were discarded, as they are likely sampling micro-inclusions. REE patterns normalized to chondrite composition (Palme and O'Neill, 2004), Eu anomaly and Th/U ratios are used as proxies to discriminate between different zircon populations (Figure 11-b).

The zircon cores are older (>400 Ma) with respect to the rims (<350 Ma) and have a distinct Th-U and REE systematic. Grain cores generally contain 50–900 ppm U and have Th/U in the range 0.28–0.99, while rims contain 2–40 ppm U and their Th/U is generally lower than 0.2. The zircon cores are around one or two orders of magnitude richer in REE than the younger zircon rims, they present slight to strong negative Eu anomalies (Eu/Eu* = 0.17–0.47) and are enriched in HREE with respect to the L–MREE (Lu–Yb concentrations ~1000 times chondrite and $(Lu/Gd)_N$ = 17–40). Zircon rims are poorer in REE with a variety of patterns ranging from flat to strongly enriched in HREE ($(Lu/Gd)_N$ from 1.4 to 614). Eu anomaly ranges from weakly negative to positive (Eu/Eu* = 0.88–1.53). There is no clear relationship between the U-Pb dates and the shape of REE profiles for the rims.

The Ti content of zircon ranges from 4.6 to 9.9 ppm in the cores, and from 1.1 to 10.0 ppm in the rims, excluding one outlier. Using the Ti-in-zircon thermometer of Ferry and Watson (2007)

assuming TiO_2 and SiO_2 saturation, this converts to T ranging from ca. 680 to 750 °C for the cores and from 570 to 750 °C for the rims. Assuming TiO_2 activity reduced to 0.5 if ilmenite was the stable Ti phase during zircon crystallization increases T estimates by ca. 70 °C (740–810°C for the cores and 620–820°C for the rims).

7.2. Zircon and rutile U-Pb dating

Most of U-Pb analyses of zircon cores are concordant (more than 95%) and yield $^{206}Pb/^{238}U$ dates in the range 470–492 Ma (Figure 12-a), with the exclusion of three younger outliers. The $^{206}Pb/^{238}U$ weighted mean age of 479±5 Ma is calculated from eight zircon cores analyses and is within uncertainty the same as the concordia age (480±5Ma, $MSWD_{(c+e)}$=1.3). Zircon rims analyses contain more common Pb (f_{206} up to 6 %) and are best displayed in the Tera-Wasserburg diagram (Figure 12-c). Analyses corrected for common Pb assuming present day $^{207}Pb/^{206}Pb$ value according to Stacey and Kramers (1975) display $^{206}Pb/^{238}U$ dates between 294 and 337 Ma (Figure 12-b). Zircon U–Pb dates present a bimodal distribution, with two main clusters around 318–326 Ma and 303–310 Ma. However, there is no discernible correlation between U–Pb dates and composition or internal texture of the zircon rims.

The rutile extracted from sample JB-19-56 contains significant common Pb, 43 analyses from 34 different grains define a linear regression in the Tera-Wasserburg diagram (Figure 12-c). The intercept age is 337±7 Ma (MSWD=1.3) and the free upper intercept for $^{207}Pb/^{206}Pb$ is 0.80±0.04. This value is within uncertainty that of the present-day value predicted by the Stacey and Kramers (1975) model.

8. DISCUSSION

8.1. Emplacement of the mafic protoliths

The zircon cores in the dated mafic granulite sample (JB-19-56) present typical features of magmatic zircon such as oscillatory or broad sector zoning, relatively high U content with respect to the rims and high Th/U (Corfu et al., 2003; Hoskin and Schaltegger, 2003). The steep REE patterns and the negative Eu anomalies are consistent with crystallization from a basaltic melt that has fractionnated plagioclase (Hoskin and Schaltegger, 2003). The Ordovician age of 479±5 Ma of the zircon cores is therefore interpreted as the crystallization age of the magmatic protolith. This age is within uncertainty the same as that obtained for zircon in a sample from the Peyre-Arguet granulite at 471±5 Ma (Fréville, 2016),

589 which suggests that these two bodies were emplaced during the same magmatic event. This Ordovician
590 age is consistent with the regional record in the ECM, where most of igneous mafic protoliths yield
591 ages between 450 and 480 Ma (Jacob et al., 2021; Paquette et al., 1989; Rubatto et al., 2010).
592 Cambrian–Ordovician magmatism is widespread in the Variscan basement of Europe (Pin and Marini,
593 1993), and is generally attributed to a regional extensional event that affected all the northern part of
594 Gondwana and resulted in the rifting of the Rheic and Saxo-Thuringian Oceans during the Early-mid-
595 Ordovician.

596 8.2. Metamorphic evolution of the HP mafic granulites

597 8.2.1. P–T evolution of La Lavey granulitic body

598 Inverse thermobarometry and forward modeling in the three samples from La Lavey provide reliable
599 constraints for five different metamorphic stages, which allow reconstructing a comprehensive P-T path
600 from the early prograde (stage 1) to the late retrograde phases (stage 5).

601 The early prograde phase (stage1) is constrained by Mn-rich garnet cores (Grt-1) in sample
602 JB-19-43, which contain inclusions of epidote, chlorite, titanite and white mica. Thermodynamic
603 modeling indicates conditions of the amphibolite-facies during stage 1 (460–550°C and 0.4–1.0 GPa),
604 which rules out possible evolution along a low-T geotherm at blueschist-facies conditions typical of
605 subduction environments. Then, progressive increase in T and P is marked by increasing modal
606 proportion of garnet, entrapment of rutile inclusion and progressive increase in Mg associated with
607 decrease in Ca from Grt-1 to Grt-2, which is observed in both samples JB-19-43 and JB-19-56. The
608 pressure peak (stage 2) is constrained at 650–730°C and 1.5–1.7 GPa based on composition of Mg-rich
609 garnet (Grt-2) and estimation of the highest jadeite content in clinopyroxene by reintegration of the
610 symplectites in sample JB-19-56.

611 Decompression following the pressure peak is associated with resorption of garnet and coarse-
612 grained clinopyroxene, which respectively break down into a polycrystalline, plagioclase-rich
613 granoblastic corona and plagioclase + clinopyroxene symplectites. Recrystallization of the symplectites
614 into a mosaic assemblage of plagioclase and clinopyroxene is observed, in particular in relict granulitic
615 domains in sample JB-19-55. These annealing textures are indicative of HT conditions during
616 decompression. They contrast with fine-grained (vermicular) symplectites commonly observed in
617 retrogressed eclogites or HP granulites, in particular in those from the other ECM of Belledonne,

Aiguilles–Rouges and Argentera (Jacob et al., 2021; Jouffray et al., 2020; Vanardois et al., 2022). Two stages of decompression are identified (stages 3 and 4), which correspond to different compositions of plagioclase (Na-rich or Ca-rich) and amphibole (Al-poor or Al-rich) measured in sample JB-19-56. They occurred at high to medium P conditions (stage 3: 1.0–1.3 GPa and 730–800 °C; stage 4: 0.6–0.9 GPa and 800–870°C), according to forward thermodynamic modeling and inverse thermobarometry performed in sample JB-19-56. According to the amount of Na vs Ca-rich plagioclase, most of the retrogression has occurred during stage 3, while stage 4 is more discrete and produced only a stealth overprint around garnet and at the plagioclase grain boundaries (Figure 5a). Stage 4 is associated with the formation of a thin garnet rim enriched in Mn (Grt-3) in contact with Ca-rich plagioclase in sample JB-19-56. This garnet overgrowth during decompression may result from local enrichment in Mn around the resorbing garnet grains.

Finally, stage 5 corresponds to late retrogression and cooling at amphibolite-facies conditions. This late stage is not observed or very discrete in the least retrogressed samples (JB-19-43 and JB-19-56), but is much more pronounced in the amphibolite sample JB-19-55. In this latter sample, it was associated with pervasive rehydration (metasomatism) and intense deformation, which resulted in development of a layered plagioclase-amphibole assemblage, which almost completely overprinted the former HT granulitic assemblage. The latter is only preserved as relics corresponding to plagioclase+clinopyroxene mosaic domains. Based on plagioclase–amphibole thermometry, this retrogression occurred over a large range of T from upper (656±33°C) to lower amphibolite facies (573±44°C).

8.2.2. Temperature constrains from Zr-in-rutile

Rutile temperatures in samples from La Lavey are consistent with this P–T evolution. Rutile inclusions in garnet yield T scattering between 611 and 775 °C: the lower end of this range is consistent with prograde entrapment of rutile in garnet between stage 1 and stage 2, while the higher end yields approximately the same T as matrix rutile, which suggests equilibration during heating and decompression. Many HT rutile inclusions display textures indicative of partial replacement by ilmenite, which suggests that this rutile re-equilibrated at HT conditions in the stability field of rutile + ilmenite (~1.0 GPa). However, in such a situation of partial replacement of rutile by ilmenite, Zr is known to remain dominantly in rutile and very few Zr is incorporated into ilmenite (Whitney et al., 2015), which leads to a local increase in Zr content in the remaining rutile. The broadly higher Zr-

content observed in this rutile may therefore result in part from this process, and would not result only from equilibration at higher T. The large spread of Zr-content in rutile inclusions is in consequence complex to interpret, and probably reflects a combination of: (i) variable P-T conditions during rutile entrapment; (ii) possible re-equilibration of Zr in rutile at higher-T during decompression, and (iii) favorable partition of Zr during replacement by ilmenite. It is important to emphasize here that the separated rutile grains that have been used for U-Pb dating do not present any trace of ilmenite replacement and display low Zr-content (<350ppm), which means they have not been affected by these processes.

Matrix rutile in samples JB-19-43 and JB-19-55 yields HT conditions (737–792 °C) consistent with equilibration during decompression at HT (stage 3). The highest Zr-in-rutile T is ca. 40°C lower than peak-T estimated from amphibole-plagioclase thermometry (833±35°C). We do not interpret this discrepancy as the result of post peak-T diffusion, first because there is not evidence of diffusion zoning in the rutile grains, and second because several studies have demonstrated that the Zr-in-rutile thermometer is robust to diffusive re-equilibration up to ultra-high T conditions (e.g. Ewing et al., 2013; Pape et al., 2016). We suggest instead that peak-T occurred in the stability field of ilmenite, and is therefore not recorded by rutile, which rather constrains T during the last step of equilibration above the Rt-out reaction between stages 3 and 4 (Figure 9).

Finally, late rutile in sample JB-19-55, which grows together with titanite in replacement of ilmenite, yields low T between 457 and 499 °C, which is ca. 50–70°C lower than T estimated for plagioclase–actinolite pairs (stage 5) and marks late retrogression to the lower amphibolite facies.

Despite a more pervasive retrogression, the samples from Peyre-Arguet share similarities with the mafic HP granulites from La Lavey. In particular, widespread occurrence of granoblastic mosaic assemblages rather than vermicular symplectites marks decompression at HT conditions following the HP stage. Textures in sample JB-19-16 correspond to an intermediate state of retrogression between the well-preserved HP granulites (JB-19-43;56) and the highly retrogressed sample JB-19-55. Rutile in samples from Peyre-Arguet displays similar features as rutile in samples from La Lavey, with high Zr-in-rutile T in matrix grains (778–818 °C) and large scattering of T in rutile inclusions in garnet (654–793°C). Consequently, the Peyre-Arguet retrogressed granulites have probably undergone a similar P–T evolution as the Lavey HP granulites, with a prograde to HP evolution at relatively moderate T (ca. 650–750 °C), followed by heating to >800 °C during decompression. However, Zr-content in rutile is

678 generally higher in samples from Peyre-Arguet than in samples from La Lavey. For the same textural
679 position (matrix or inclusions), the distribution of Zr-in-rutile data is shifted by 50 to 300 ppm toward
680 higher values in Peyre-Arguet, which may reflect slightly higher peak-P (+0.4 GPa) and/or peak-T
681 (+20°C) conditions.

682 8.3. Timing of the metamorphic evolution

683 Rutile from sample JB-19-56 yields an age at 337 ± 7 Ma, which is older than most of U-Pb dates
684 obtained in zircon rims of this study and predates by 30 to 40 Ma the widespread HT migmatitic event
685 recorded in the inner zone of the Oisans–Pelvoux massif (Fréville, 2016, see compilation of U-Pb data
686 on Figure 13). We therefore attribute the age at 337 ± 7 Ma to an early HP metamorphic stage that
687 predates HT decompression, rather than a cooling age after the thermal peak, which would be
688 inconsistent with the regional geochronological record.

689 Preservation of an early crystallization age in rutile is unexpected, given that Pb diffusion in
690 rutile is considered to be relatively fast at T over 600–650°C (Cherniak, 2000; Zack and Kooijman,
691 2017). However, this is not an isolated observation. Similar rutile ages around 340 Ma have also been
692 attributed to the HP stage in retrogressed Variscan eclogites from the neighboring massifs of
693 Belledonne (Jacob et al., 2021) and Aiguilles–Rouges (Vanardois et al., 2022), despite contrasted
694 exhumation path at T>700-750°C (see section 8.5 below).. Low Zr-content and lack of ilmenite
695 exsolution or replacement in the dated rutile grains (Figures 10-a and 11-a) indicate lack of re-
696 equilibration during HT decompression, probably due to shielding in garnet. Therefore, we tentatively
697 attribute this unusual preservation of early metamorphic ages in rutile ages to the shielding effect of
698 garnet, which may prevent both fluid access to the rutile inclusions and diffusional Pb-loss (Dahl,
699 1997). Similar preservation of prograde rutile ages due to shielding in garnet has been reported in
700 different settings (e.g; Bruguier et al., 2017), although this effect is not systematic (Zhou et al., 2020).

701 Zircon rims generally display low U and low Th/U ratios, they are depleted in REE with
702 respect to the zircon cores and they form homogeneous CC bright domains, which are typical features
703 of metamorphic zircon formed under sub-solidus conditions (Hoskin and Schaltegger, 2003; Rubatto,
704 2017). U–Pb dates cover a wide range between 294 and 337 Ma, with two main clusters at 326–318 Ma
705 and 310–303 Ma. This suggests that zircon rims have crystallized during a protracted period, either
706 continuously or during multiple episodes. The large variety of zircon REE patterns, which do not
707 correlate with U-Pb dates, suggests chemical disequilibrium for REE between different domains during

zircon growth. Flat HREE patterns are indicative of growth in a garnet-rich bulk, which fractionates HREE (Rubatto, 2002), while enrichment in HREE rather indicates zircon growth associated with garnet-breakdown. The HREE-enriched rims likely formed in portions of the rock where the garnet-bearing HP assemblage was resorbing and releasing HREE, while the HREE-flat rims formed in portions of the rock where retrogression was less pronounced. Correspondingly, the lack of a significant negative Eu anomaly in the zircon rims is not taken to signify lack of plagioclase in the assemblage, but rather disequilibrium growth (e.g. Lotout et al., 2018).

Ti-in-zircon thermometry yields scattering temperatures, that are uncorrelated with U-Pb dates and are broadly 50 to 100 °C lower than maximal Zr-in-rutile temperatures. This shift suggests rutile and zircon growth are decorrelated and correspond to different stages of the P-T evolution. The apparently lower T in zircon may result from crystallization under reduced a_{TiO2} conditions, either at lower P in the ilmenite stability field, or due to incomplete equilibration of Ti at the sample scale. Overall, the relatively large range of zircon ages combined with non-systematic trace elements patterns does not allow dating a precise P-T stage but rather indicates metamorphic zircon growth between ca. 340 and 295 Ma, broadly under decompression as attested by some HREE-enriched rims.

8.4. Evolution at the regional scale

Comparison of the zircon rims ages from this study with data from the surrounding metamorphic rocks provides insight into the metamorphic evolution of the Oisans–Pelvoux massif. A summary of geochronological data from Fréville (2016) and this work is presented in Figure 13. The data were split by domains between the widely migmatized inner Oisans-Pelvoux zone and the lower grade cortical zone in the western part of the massif (Figure 1). The distribution of zircon and monazite U-Pb dates in the high grade inner zone marks three distinct peaks corresponding to the Visean (ca. 340 –325 Ma), the Late Carboniferous – Early Permian (ca. 310–295 Ma) and the mid-Permian (ca. 285–270 Ma). Only the Visean peak is recorded in the lower grade cortical zone, which does not display any trace of younger events.

Excluding the late mid-Permian stage, the regional timing of metamorphism is consistent with that recorded in the HP granulites: the rutile age at 337±7 Ma plots in the older end of the Visean peak and zircon rims U–Pb dates spread from the Visean to the late Carboniferous – early Permian peak. Dated rutile yields low Zr-in-rutile T consistent with the prograde evolution and zircon rims are interpreted to have formed during broad decompression and heating to HT conditions (stages 3 and 4 of

738 the metamorphic evolution). Therefore, we correlate the Visean peak with the period of nappe stacking
739 and crustal thickening (D1 regional phase), during which upper and mid-crustal units of both the inner
740 and the cortical zone were buried. The upper Carboniferous – early Permian peak is in turn interpreted
741 to date heating to HT conditions during exhumation, which is only recorded in the inner zone of the
742 Oisans–Pelvoux massif and matches with the emplacement age of most of granite intrusions in this
743 domain (Fréville, 2016).

744 Interestingly, nearly all zircon of the younger populations (late Carboniferous and Permian)
745 display high Th/U > 0.1 (Figure 13b), while older zircons display more scattered Th/U between 0.001
746 and 1. High Th/U are generally indicative of crystallization in equilibrium with a melt (Hoskin and
747 Schaltegger, 2003), and therefore the lack of low Th/U zircon in the late Carboniferous population,
748 comparatively with older zircon, is another indication of a HT migmatitic environment during this
749 period. This strongly suggests that HT decompression observed in the HP granulites, emplacement of
750 granitoids and migmatization of the inner Oisans–Pelvoux zone occurred during the same late
751 Carboniferous – early Permian (ca. 310–295 Ma) HT event.

752 ## 8.5. Thermal state of the Variscan crust and possible geodynamic scenario

753

754 Until recently (Guillot and Ménot, 2009, Fréville et al., 2018), Variscan eclogites and HP granulites in
755 the ECM were regarded as the relics of Cambrian-Ordovician oceanic crust subducted during the
756 Devonian (ca. 390-400 Ma), based on ID-TIMS ages on multigrain fractions of zircon obtained by
757 Paquette et al. (1989). However, both the age and P-T conditions of HP metamorphism are in
758 contradiction with this interpretation.

759 First, all HP relics in the ECM record a similar timing for prograde to peak-P metamorphism around
760 345-330 Ma (Jacob et al., 2021; Jouffray et al., 2020; Vanardois et al., 2022, this work), which is
761 inconsistent with a Devonian subduction. This timing matches instead with that of the barrovian
762 metamorphic sequence observed in the southern Belledonne massif and the cortical zone of the Oisans–
763 Pelvoux massif, which corresponds to burying of the Devonian–Tournaisian arc/back-arc series to ca.
764 0.6-0.9 GPa and 650–700°C (Fréville, 2016; Fréville et al., 2018; Guillot and Ménot, 1999). Therefore,
765 the HP stage in the ECM marks a regional MT/HP event, that we correlate to the regional D1 nappe
766 stacking.

767 Then, metamorphic P–T conditions estimated for the mafic HP granulites from La Lavey allow to
768 constrain the local geotherm during the different stages of the metamorphic evolution. Assuming a
769 crustal density of 2800 kg.m^{-3}, we estimate that early burial of the mid-crustal metamorphic nappes
770 (stage 1) occurred along a relatively mild local geothermal gradient (ca. 12-19°C.km^{-1}). Peak-P
771 conditions (stage 2) were reached at ca. 55–60 km depth along a mean gradient of 12–13 °C.km^{-1}, and
772 exhumation stages 3 and 4 mark progressive re-equilibration along a much warmer local geotherm (ca.
773 25–38 °C.km^{-1}).

774 Early prograde stage 1 thus occurred in a middle crust at upper greenschist-facies conditions, which
775 then reached conditions of the HP granulite-facies during stage 2. The apparent gradient during the
776 early metamorphic stages is significantly higher than what is commonly recorded during subduction of
777 a cold passive margin (< 10°C/km, Maruyama, 1996).

778 This result is in line with early emplacement of granitoids during the Visean (345-335 Ma), barely 5 to
779 10 Ma after the onset of collision. This implies that the crust was already relatively hot and prone to
780 melting during the early collisional stages, due to thermal inheritance from Devonian arc/back-arc
781 magmatism, which was active from ca. 370 to 350 Ma in the ECM (Fréville et al., 2018; Guillot and
782 Ménot, 2009; Ménot, 1987). We therefore suggest that the regional phase D1 corresponds to the
783 inversion of a Devonian continental back-arc during collision, which resulted in HP metamorphism at
784 MT/HT conditions.

785

786

787 Post peak-P heating to HT granulite-facies conditions (>800 °C) during the late Carboniferous
788 is only recorded in the inner zone of the Oisans–Pelvoux massif. In contrast, peak-T conditions in
789 metamorphic series exposed in the cortical Oisans–Pelvoux zone and in the southern Belledonne massif
790 (Figure 1) do not exceed 650–700 °C at 0.6–0.9 GPa (Fréville et al., 2018; Guillot and Menot, 1999).
791 All the other eclogites relics in the ECM (Belledonne, Argentera, Aiguilles–Rouges) record peak-T
792 around 700–750 °C (Jacob et al., 2021; Jouffray et al., 2020; Vanardois et al., 2022). Furthermore, the
793 geochronological record in the cortical zone of Oisans–Pelvoux does not reveal any sign of a late
794 Carboniferous HT overprint (Figure 13a). We interpret the lack of HT overprint in these domains as the
795 result of relatively rapid exhumation to upper structural levels after peak-P. In contrast, the inner zone
796 of the Oisans–Pelvoux massif has remained in the lower crust until the late Carboniferous (310–300

Ma), where it has been heated to HT conditions. Our thermobarometric estimations indicate that peak-T was reached in the lower crust (ca. 20–30 km; 0.6–0.9 GPa). Heating could have occurred progressively during decompression from stage 2 to stage 4, due to thermal maturation of the lower crust. However, given the relatively stealth overprint of the HP granulites during stage 4 and the episodic growth of zircon and monazite in the metamorphic basement, we suggest that the HT overprint was relatively short-lived and occurred after a first step of decompression from high to middle-P conditions. The two possible exhumation paths (progressive heating during decompression or sharp T increase after decompression) are shown with dotted lines on Figure 13. Cordierite is found is the surrounding felsic migmatites (Figure S1 in the supplements), which indicates HT conditions at lower P than recorded for stage 4 in the HP granulites (<0.6 GPa, White et al., 2001). This may result from the juxtaposition of high-grade crustal units coming from different structural levels of the lower to middle crust, which were exhumed together in a domal structure. This setting is similar for instance to the Montagne Noire Axial Zone (Whitney et al., 2020), which presents similar features.

The sharp increase of T (ca. 100–200 °C) between stage 2 (peak-P) and stage 4 (peak-T) requires important heat input, especially when considering that a significant part of the additional thermal energy has been pumped out in melting reactions to form the large volumes of granite (Moyen, 2019). Part of this thermal energy comes from internal radiogenic heat production in the thickened orogenic crust. However, the metamorphic pile in the Oisans–Pelvoux massif contains large amounts of amphibolite and amphibolitic gneiss poor in radioactive elements, and the ca. 30 Ma interval between peak-P and peak-T may have therefore been too short to produce this thermal overprint accounting only for internal crustal heat sources (Bea, 2012; Clark et al., 2011). Mantle-derived (ultra)-potassic magmatic rocks akin to the durbachites and vaugnerites series (Von Raumer et al., 2014) are ubiquitous in the basement (Figure 1) and may have contributed to heating, either by underplating below the lower crust or by intruding directly in the lower crust. Finally, upwelling of hot asthenospheric mantle in response of slab rollback or lithospheric delamination during the post-collisional stages may be a possible source for additional heating, as suggested in the French Massif Central or the Bohemian Massif (e.g. Vanderhaeghe et al., 2020; Žák et al., 2018).

9. CONCLUSION

High-pressure mafic granulite that were newly identified in the Oisans–Pelvoux massif represents an invaluable material to infer the P-T-t evolution of this widely migmatized massif that records the

highest metamorphic conditions in the external crystalline massifs of the French Alps. The mafic HP granulites derive from ordovician tholeiitic protoliths emplaced at 479±5 Ma. They preserve the relics of multiple Variscan metamorphic stages, from an early prograde phase at 460–550 °C and 0.4–1.0 GPa to peak P conditions at 650–730 °C and 1.5–1.7 GPa. The HP assemblage was then destabilized at HT conditions during decompression and peak T of 800–870°C was reached at 0.6–0.9 GPa. In the best-preserved mafic HP granulites, lack of strong fluid-input during cooling allowed preservation of the HP and HT assemblages, and no subsequent retrogression stage is recorded. In contrast, the most retrogressed samples have undergone pervasive deformation and metasomatism that were associated with crystallization of an amphibolitic assemblage from ca. 690 °C to 450 °C.

The timing of the Variscan metamorphic evolution is constrained by a U-Pb age on rutile at 337±7 Ma and by U–Pb dates of metamorphic zircon rims scattered between 337 and 294 Ma. Most of zircon rims have crystallized during decompression, and therefore the older rutile age is interpreted to date prograde or HP stages. The timing and P–T conditions of prograde to HP evolution are comparable with those of other HP rocks in the ECM, and correspond to burying of continental units along a medium-T geothermal gradient (ca. 12–13 °C.km-1). Upper greenschist-facies conditions during the early prograde stage are inconsistent with subduction of a cold passive margin. We therefore ascribe the prograde to HP evolution to thickening of a relatively hot continental crust, presumably caused by inversion of a Devonian back-arc during the collision.

The HP rocks of the Oisans–Pelvoux massif are the only ones in the ECM to record heating to HT granulitic conditions during decompression. Therefore, we suppose that unlike most other HP relics in the ECM, these mafic HP granulites remained stored in the lower crust for a longer period, and recorded a late heating stage possibly triggered by a combination od underplating and /or intrusion of hot mantle magmas and increased basal conductive heat flux caused by asthenospheric upwelling.

ACKNOWLEDGEMENTS

This work was supported by the BRGM through the Référentiel Géologique de la France program (RGF). J-B Jacob was funded by a doctoral grant from the ENS de Lyon. We wish to thank all the technical staff at ISTerre in Grenoble, UNIL in Lausanne and at the University of Bern, who greatly helped for the preparation of samples and during the multiple analytical sessions. This manuscript also

benefited from interesting and constructive reviews by Julien Berger and an anonymous reviewer, and from editorial handling and advice from Nadia Malaspina. Most of the field investigations were carried out in the central zone of the Ecrins National park, in which collecting rock samples is usually strictly forbidden. We therefore wish to thank the administration staff of the Ecrins National park, who gave us authorization to collect the samples and followed with great interest the advancement of this work.

REFERENCES

Axelsson, E., Pape, J., Berndt, J., Corfu, F., Mezger, K., Raith, M.M., 2018. Rutile R632 - A New Natural Reference Material for U-Pb and Zr Determination. Geostand Geoanal Res 42, 319–338. https://doi.org/10.1111/ggr.12213

Ballèvre, M., Manzotti, P., Piaz, G.V.D., 2018. Pre-Alpine (Variscan) Inheritance: A Key for the Location of the Future Valaisan Basin (Western Alps). Tectonics 37, 786–817. https://doi.org/10.1002/2017TC004633

Ballèvre, M., Martínez Catalán, J.R., López-Carmona, A., Pitra, P., Abati, J., Fernández, R.D., Ducassou, C., Arenas, R., Bosse, V., Castiñeiras, P., Fernández-Suárez, J., Gómez Barreiro, J., Paquette, J.-L., Peucat, J.-J., Poujol, M., Ruffet, G., Sánchez Martínez, S., 2014. Correlation of the nappe stack in the Ibero-Armorican arc across the Bay of Biscay: a joint French–Spanish project. Geological Society, London, Special Publications 405, 77–113. https://doi.org/10.1144/SP405.13

Bea, F., 2012. The sources of energy for crustal melting and the geochemistry of heat-producing elements. Lithos 153, 278–291.

Bellahsen, N., Mouthereau, F., Boutoux, A., Bellanger, M., Lacombe, O., Jolivet, L., Rolland, Y., 2014. Collision kinematics in the western external Alps. Tectonics 33, 1055–1088. https://doi.org/10.1002/2013TC003453

Bellanger, M., Augier, R., Bellahsen, N., Jolivet, L., Monié, P., Baudin, T., Beyssac, O., 2015. Shortening of the European Dauphinois margin (Oisans Massif, Western Alps): New insights from RSCM maximum temperature estimates and 40Ar/39Ar in situ dating. Journal of Geodynamics 83, 37–64. https://doi.org/10.1016/j.jog.2014.09.004

Black, L.P., Kamo, S.L., Allen, C.M., Aleinikoff, J.N., Davis, D.W., Korsch, R.J., Foudoulis, C., 2003. TEMORA 1: a new zircon standard for Phanerozoic U–Pb geochronology. Chemical Geology 200, 155–170. https://doi.org/10.1016/S0009-2541(03)00165-7

Carignan, J., Hild, P., Mevelle, G., Morel, J., Yeghicheyan, D., 2001. Routine Analyses of Trace Elements in Geological Samples using Flow Injection and Low Pressure On-Line Liquid Chromatography Coupled to ICP-MS: A Study of Geochemical Reference Materials BR, DR-N, UB-N, AN-G and GH. Geostandards Newsletter 25, 187–198. https://doi.org/10.1111/j.1751-908X.2001.tb00595.x

Cherniak, D.J., 2000. Pb diffusion in rutile. Contrib Mineral Petrol 139, 198–207. https://doi.org/10.1007/PL00007671

Chew, D.M., Petrus, J.A., Kamber, B.S., 2014. U–Pb LA–ICPMS dating using accessory mineral standards with variable common Pb. Chemical Geology 363, 185–199. https://doi.org/10.1016/j.chemgeo.2013.11.006
Clark, C., Fitzsimons, I.C.W., Healy, D., Harley, S.L., 2011. How Does the Continental Crust Get Really Hot? Elements 7, 235–240. https://doi.org/10.2113/gselements.7.4.235
Connolly, J.A.D., 2009. The geodynamic equation of state: What and how. Geochemistry, Geophysics, Geosystems 10, n/a-n/a. https://doi.org/10.1029/2009GC002540
Corfu, F., Hanchar, J.M., Hoskin, P.W., Kinny, P., 2003. Atlas of zircon textures. Reviews in mineralogy and geochemistry 53, 469–500.
Dahl, P.S., 1997. A crystal-chemical basis for Pb retention and fission-track annealing systematics in U-bearing minerals, with implications for geochronology. Earth and Planetary Science Letters 150, 277–290. https://doi.org/10.1016/S0012-821X(97)00108-8
Debon, F., Lemmet, M., 1999. Evolution of Mg/Fe Ratios in Late Variscan Plutonic Rocks from the External Crystalline Massifs of the Alps (France, Italy, Switzerland). J Petrology 40, 1151–1185. https://doi.org/10.1093/petroj/40.7.1151
Duesterhoeft, E., Lanari, P., 2020. Iterative thermodynamic modelling—Part 1: A theoretical scoring technique and a computer program (Bingo-Antidote). Journal of Metamorphic Geology 38, 527–551. https://doi.org/10.1111/jmg.12538
Ewing, T.A., Hermann, J., Rubatto, D., 2013. The robustness of the Zr-in-rutile and Ti-in-zircon thermometers during high-temperature metamorphism (Ivrea-Verbano Zone, northern Italy). Contrib Mineral Petrol 165, 757–779. https://doi.org/10.1007/s00410-012-0834-5
Fernandez, A., Guillot, S., Ménot, R.-P., Ledru, P., 2002. Late Paleozoic polyphased tectonics in the SW Belledonne massif (external crystalline massifs, French Alps). Geodinamica Acta 15, 127–139.
Ferry, J.M., Watson, E.B., 2007. New thermodynamic models and revised calibrations for the Ti-in-zircon and Zr-in-rutile thermometers. Contrib Mineral Petrol 154, 429–437. https://doi.org/10.1007/s00410-007-0201-0
Fréville, K., 2016. L'orogenèse varisque dans les massifs cristallins externes de Belledonne et du Pelvoux (Alpes occidentales françaises) : rôle de la fusion partielle et du plutonisme dans la structuration de la croûte continentale (PhD Thesis). Université d'Orléans.
Fréville, K., Trap, P., Faure, M., Melleton, J., Li, X.-H., Lin, W., Blein, O., Bruguier, O., Poujol, M., 2018. Structural, metamorphic and geochronological insights on the Variscan evolution of the Alpine basement in the Belledonne Massif (France). Tectonophysics 726, 14–42.
Fuhrman, M.L., Lindsley, D.H., 1988. Ternary-feldspar modeling and thermometry. American mineralogist 73, 201–215.
Gale, A., Dalton, C.A., Langmuir, C.H., Su, Y., Schilling, J.-G., 2013. The mean composition of ocean ridge basalts. Geochemistry, Geophysics, Geosystems 14, 489–518. https://doi.org/10.1029/2012GC004334
Grandjean, V., Guillot, S., Pecher, A., 1996. A new record of the LP-HT late-Variscan metamorphism: The Peyre-Arguet unit (Haut-Dauphine). Comptes Rendus de l'académie des sciences 322, 189–195.
Green, E., Holland, T., Powell, R., 2007. An order-disorder model for omphacitic pyroxenes in the system jadeite-diopside-hedenbergite-acmite, with applications to eclogitic rocks. American Mineralogist 92, 1181–1189.
Green, E.C.R., White, R.W., Diener, J.F.A., Powell, R., Holland, T.J.B., Palin, R.M., 2016. Activity–composition relations for the calculation of partial melting equilibria in metabasic rocks. Journal of Metamorphic Geology 34, 845–869. https://doi.org/10.1111/jmg.12211

Guillot, S., di Paola, S., Ménot, R.-P., Ledru, P., Spalla, M.I., Gosso, G., Schwartz, S., 2009. Suture zones and importance of strike-slip faulting for Variscan geodynamic reconstructions of the External Crystalline Massifs of the western Alps. Bulletin de la Société géologique de France 180, 483–500.

Guillot, S., Menot, R., 1999. Nappe stacking and first evidence of Late Variscan extension in the Belledonne Massif (External Crystalline Massifs, French Alps). Geodinamica Acta 12, 97–111. https://doi.org/10.1016/S0985-3111(99)80026-6

Guillot, S., Ménot, R.-P., 2009. Paleozoic evolution of the External Crystalline Massifs of the Western Alps. Comptes Rendus Geoscience 341, 253–265. https://doi.org/10.1016/j.crte.2008.11.010

Holland, T., Blundy, J., 1994. Non-ideal interactions in calcic amphiboles and their bearing on amphibole-plagioclase thermometry. Contr. Mineral. and Petrol. 116, 433–447. https://doi.org/10.1007/BF00310910

Holland, T.J.B., Powell, R., 2011. An improved and extended internally consistent thermodynamic dataset for phases of petrological interest, involving a new equation of state for solids. Journal of Metamorphic Geology 29, 333–383. https://doi.org/10.1111/j.1525-1314.2010.00923.x

Holland, T.J.B., Powell, R.T.J.B., 1998. An internally consistent thermodynamic data set for phases of petrological interest. Journal of metamorphic Geology 16, 309–343.

Hoskin, P.W.O., Schaltegger, U., 2003. The Composition of Zircon and Igneous and Metamorphic Petrogenesis. Reviews in Mineralogy and Geochemistry 53, 27–62. https://doi.org/10.2113/0530027

Jacob, J.-B., Guillot, S., Rubatto, D., Janots, E., Melleton, J., Faure, M., 2021. Carboniferous high pressure metamorphism and deformation in the Belledonne Massif (Western Alps). Journal of Metamorphic Geology n/a. https://doi.org/10.1111/jmg.12600

Jochum, K.P., Nohl, U., Herwig, K., Lammel, E., Stoll, B., Hofmann, A.W., 2005. GeoReM: A New Geochemical Database for Reference Materials and Isotopic Standards. Geostandards and Geoanalytical Research 29, 333–338. https://doi.org/10.1111/j.1751-908X.2005.tb00904.x

Jochum, K.P., Weis, U., Stoll, B., Kuzmin, D., Yang, Q., Raczek, I., Jacob, D.E., Stracke, A., Birbaum, K., Frick, D.A., Günther, D., Enzweiler, J., 2011. Determination of Reference Values for NIST SRM 610–617 Glasses Following ISO Guidelines. Geostandards and Geoanalytical Research 35, 397–429. https://doi.org/10.1111/j.1751-908X.2011.00120.x

Jouffray, F., Spalla, M.I., Lardeaux, J.M., Filippi, M., Rebay, G., Corsini, M., Zanoni, D., Zucali, M., Gosso, G., 2020. Variscan eclogites from the Argentera–Mercantour Massif (External Crystalline Massifs, SW Alps): a dismembered cryptic suture zone. Int J Earth Sci (Geol Rundsch). https://doi.org/10.1007/s00531-020-01848-2

Kohn, M.J., 2020. A refined zirconium-in-rutile thermometer. American Mineralogist 105, 963–971. https://doi.org/10.2138/am-2020-7091

Lanari, P., Vho, A., Bovay, T., Airaghi, L., Centrella, S., 2018. Quantitative compositional mapping of mineral phases by electron probe micro-analyser. Geological Society, London, Special Publications 478, SP478.4. https://doi.org/10.1144/SP478.4

Lanari, P., Vidal, O., De Andrade, V., Dubacq, B., Lewin, E., Grosch, E.G., Schwartz, S., 2014. XMapTools: A MATLAB©-based program for electron microprobe X-ray image processing and geothermobarometry. Computers & Geosciences 62, 227–240. https://doi.org/10.1016/j.cageo.2013.08.010

Le Fort, P., 1971. Géologie du Haut-Dauphiné cristallin (Alpes Française): Etudes pétrologique et structurale de la partie occidentale (PhD Thesis). Université Nancy I.

Lotout, C., Pitra, P., Poujol, M., Anczkiewicz, R., Van Den Driessche, J., 2018. Timing and duration of Variscan high-pressure metamorphism in the French Massif Central: A multimethod

geochronological study from the Najac Massif. Lithos 308–309, 381–394. https://doi.org/10.1016/j.lithos.2018.03.022
Luvizotto, G.L., Zack, T., Meyer, H.P., Ludwig, T., Triebold, S., Kronz, A., Münker, C., Stockli, D.F., Prowatke, S., Klemme, S., Jacob, D.E., von Eynatten, H., 2009. Rutile crystals as potential trace element and isotope mineral standards for microanalysis. Chemical Geology, Accessory minerals as tracers of crustal processes 261, 346–369. https://doi.org/10.1016/j.chemgeo.2008.04.012
Marquer, D., Calcagno, P., Barfety, J.-C., Baudin, T., 2006. 3D Modeling and Kinematics of the External Zone of the French Western Alps (Belledonne and Grand Châtelard Massifs, Maurienne Valley, Savoie). Eclogae geol. Helv. 99, 211–222. https://doi.org/10.1007/s00015-006-1183-z
Maruyama, S., 1996. Blueschist/Eclogites of the world and their exhumation. International Geological Review 38, 490–596.
Ménot, R.-P., 1987. Magmatismes paléozoiques et structuration carbonifère du Massif de Belledonne (Alpes Françaises). Contraintes nouvelles pour les schémas d'évolution de la chaîne varisque ouest-européenne. Université Claude Bernard Lyon 1.
Moyen, J.-F., 2019. Granites and crustal heat budget. Geological Society, London, Special Publications 491, SP491-2018–148. https://doi.org/10.1144/SP491-2018-148
O'Brien, P.J., Rötzler, J., 2003. High-pressure granulites: formation, recovery of peak conditions and implications for tectonics. Journal of Metamorphic Geology 21, 3–20. https://doi.org/10.1046/j.1525-1314.2003.00420.x
Palme, H., O'Neill, H.S., 2004. C. 2014. Cosmochemical estimates of mantle composition. Treatise on Geochemistry. Oxford: Elsevier-Pergamon 1–39.
Pape, J., Mezger, K., Robyr, M., 2016. A systematic evaluation of the Zr-in-rutile thermometer in ultra-high temperature (UHT) rocks. Contrib Mineral Petrol 171, 44. https://doi.org/10.1007/s00410-016-1254-8
Paquette, J.L., Menot, R.P., Peucat, J.J., 1989. REE, Sm-Nd and U-Pb zircon study of eclogites from the Alpine External Massifs (Western Alps): evidence for crustal contamination. Earth and Planetary Science Letters 96, 181–198.
Paton, C., Hellstrom, J., Paul, B., Woodhead, J., Hergt, J., 2011. Iolite: Freeware for the visualisation and processing of mass spectrometric data. Journal of Analytical Atomic Spectrometry 26, 2508–2518. https://doi.org/10.1039/C1JA10172B
Pecher, A., 1970. Etude pétrographique de la partie orientale du massif des Ecrins-Pelvoux: le socle ancien - Alpes françaises.
Pin, C., Marini, F., 1993. Early Ordovician continental break-up in Variscan Europe: Nd-Sr isotope and trace element evidence from bimodal igneous associations of the Southern Massif Central, France. Lithos 29, 177–196. https://doi.org/10.1016/0024-4937(93)90016-6
Pitra, P., Poujol, M., Van Den Driessche, J., Bretagne, E., Lotout, C., Cogné, N., Harley, S., 2021. Late Variscan (315 Ma) subduction or deceptive zircon REE patterns and U–Pb dates from migmatite-hosted eclogites? (Montagne Noire, France). J Metamorph Geol jmg.12609. https://doi.org/10.1111/jmg.12609
Rossi, P., Oggiano, G., Cocherie, A., 2009. A restored section of the "southern Variscan realm" across the Corsica–Sardinia microcontinent. Comptes Rendus Geoscience 341, 224–238.
Rubatto, D., 2017. Zircon: the metamorphic mineral. Reviews in mineralogy and geochemistry 83, 261–295.

Rubatto, D., 2002. Zircon trace element geochemistry: partitioning with garnet and the link between U–Pb ages and metamorphism. Chemical Geology 184, 123–138. https://doi.org/10.1016/S0009-2541(01)00355-2
Rubatto, D., Ferrando, S., Compagnoni, R., Lombardo, B., 2010. Carboniferous high-pressure metamorphism of Ordovician protoliths in the Argentera Massif (Italy), Southern European Variscan belt. Lithos 116, 65–76.
Simonetti, M., Carosi, R., Montomoli, C., Cottle, J.M., Law, R.D., 2020. Transpressive Deformation in the Southern European Variscan Belt: New Insights From the Aiguilles Rouges Massif (Western Alps). Tectonics 39, e2020TC006153. https://doi.org/10.1029/2020TC006153
Simonetti, M., Carosi, R., Montomoli, C., Langone, A., D'Addario, E., Mammoliti, E., 2018. Kinematic and geochronological constraints on shear deformation in the Ferriere-Mollières shear zone (Argentera-Mercantour Massif, Western Alps): implications for the evolution of the Southern European Variscan Belt. Int J Earth Sci (Geol Rundsch) 107, 2163–2189. https://doi.org/10.1007/s00531-018-1593-y
Sláma, J., Košler, J., Condon, D.J., Crowley, J.L., Gerdes, A., Hanchar, J.M., Horstwood, M.S.A., Morris, G.A., Nasdala, L., Norberg, N., Schaltegger, U., Schoene, B., Tubrett, M.N., Whitehouse, M.J., 2008. Plešovice zircon — A new natural reference material for U–Pb and Hf isotopic microanalysis. Chemical Geology 249, 1–35. https://doi.org/10.1016/j.chemgeo.2007.11.005
Stacey, J., Kramers, J., 1975. Approximation of terrestrial lead isotope evolution by a two-stage model. Earth and planetary science letters 26, 207–221.
Steiger, R.H., Jäger, E., 1977. Subcommission on geochronology: Convention on the use of decay constants in geo- and cosmochronology. Earth and Planetary Science Letters 36, 359–362. https://doi.org/10.1016/0012-821X(77)90060-7
Thompson, A.B., England, P.C., 1984. Pressure—Temperature—Time Paths of Regional Metamorphism II. Their Inference and Interpretation using Mineral Assemblages in Metamorphic Rocks. Journal of Petrology 25, 929–955. https://doi.org/10.1093/petrology/25.4.929
Vanardois, J., Roger, F., Trap, P., Goncalves, P., Lanari, P., Paquette, J.-L., Marquer, D., Cagnard, F., Le Bayon, B., Melleton, J., Barou, F., 2022. Exhumation of deep continental crust in a transpressive regime: the example of Variscan eclogites from the Aiguilles-Rouges Massif (Western Alps). Journal of Metamorphic Geology n/a. https://doi.org/10.1111/jmg.12659
Vanderhaeghe, O., Laurent, O., Gardien, V., Moyen, J.-F., Gébelin, A., Chelle-Michou, C., Couzinié, S., Villaros, A., Bellanger, M., 2020. Flow of partially molten crust controlling construction, growth and collapse of the Variscan orogenic belt: the geologic record of the French Massif Central. Bulletin de la Société Géologique de France 191. https://doi.org/10.1051/bsgf/2020013
Vielzeuf, D., Holloway, J.R., 1988. Experimental determination of the fluid-absent melting relations in the pelitic system. Contr. Mineral. and Petrol. 98, 257–276. https://doi.org/10.1007/BF00375178
Von Raumer, J.F., Bussy, F., Schaltegger, U., Schulz, B., Stampfli, G.M., 2013. Pre-Mesozoic Alpine basements—their place in the European Paleozoic framework. Bulletin of the Geological Society of America 125, 89–108.
Von Raumer, J.F., Bussy, F., Stampfli, G.M., 2009. The Variscan evolution in the External massifs of the Alps and place in their Variscan framework. Comptes Rendus Geoscience 341, 239–252. https://doi.org/10.1016/j.crte.2008.11.007
Von Raumer, J.F., Finger, F., Veselá, P., Stampfli, G.M., 2014. Durbachites–Vaugnerites–a geodynamic marker in the central E uropean Variscan orogen. Terra Nova 26, 85–95.

Watt, G.R., Griffin, B.J., Kinny, P.D., 2000. Charge contrast imaging of geological materials in the environmental scanning electron microscope. American Mineralogist 85, 1784–1794. https://doi.org/10.2138/am-2000-11-1221

White, R.W., Powell, R., Holland, T.J.B., 2001. Calculation of partial melting equilibria in the system Na2O–CaO–K2O–FeO–MgO–Al2O3–SiO2–H2O (NCKFMASH). Journal of Metamorphic Geology 19, 139–153. https://doi.org/10.1046/j.0263-4929.2000.00303.x

White, R.W., Powell, R., Holland, T.J.B., Johnson, T.E., Green, E.C.R., 2014. New mineral activity–composition relations for thermodynamic calculations in metapelitic systems. Journal of Metamorphic Geology 32, 261–286. https://doi.org/10.1111/jmg.12071

White, R.W., Powell, R., Holland, T.J.B., Worley, B.A., 2000. The effect of TiO2 and Fe2O3 on metapelitic assemblages at greenschist and amphibolite facies conditions: mineral equilibria calculations in the system K2O-FeO-MgO-Al2O3-SiO2-H2O-TiO2-Fe2O3. Journal of Metamorphic Geology 18, 497–511.

Whitney, D.L., Hamelin, C., Teyssier, C., Raia, N.H., Korchinski, M.S., Seaton, N.C.A., Bagley, B.C., Handt, A. von der, Roger, F., Rey, P.F., 2020. Deep crustal source of gneiss dome revealed by eclogite in migmatite (Montagne Noire, French Massif Central). Journal of Metamorphic Geology 38, 297–327. https://doi.org/10.1111/jmg.12523

Whitney, D.L., Roger, F., Teyssier, C., Rey, P.F., Respaut, J.-P., 2015. Syn-collapse eclogite metamorphism and exhumation of deep crust in a migmatite dome: The P–T–t record of the youngest Variscan eclogite (Montagne Noire, French Massif Central). Earth and Planetary Science Letters 430, 224–234. https://doi.org/10.1016/j.epsl.2015.08.026

Wiedenbeck, M., Hanchar, J.M., Peck, W.H., Sylvester, P., Valley, J., Whitehouse, M., Kronz, A., Morishita, Y., Nasdala, L., Fiebig, J., Franchi, I., Girard, J.-P., Greenwood, R.C., Hinton, R., Kita, N., Mason, P.R.D., Norman, M., Ogasawara, M., Piccoli, P.M., Rhede, D., Satoh, H., Schulz-Dobrick, B., Skår, O., Spicuzza, M., Terada, K., Tindle, A., Togashi, S., Vennemann, T., Xie, Q., Zheng, Y.-F., 2004. Further Characterisation of the 91500 Zircon Crystal. Geostandards and Geoanalytical Research 28, 9–39. https://doi.org/10.1111/j.1751-908X.2004.tb01041.x

Zack, T., Kooijman, E., 2017. Petrology and Geochronology of Rutile. Reviews in Mineralogy and Geochemistry 83, 443–467. https://doi.org/10.2138/rmg.2017.83.14

Žák, J., Svojtka, M., Opluštil, S., 2018. Topographic inversion and changes in the sediment routing systems in the Variscan orogenic belt as revealed by detrital zircon and monazite UPb geochronology in post-collisional continental basins. Sedimentary Geology 377, 63–81. https://doi.org/10.1016/j.sedgeo.2018.09.008

SUPPORTING INFORMATION

Additional Supporting Information may be found online in the supporting information tab for this article.

Figure S1. Field pictures of migmatitic textures in the felsic (a–b) and intermediate / mafic (c–d) protoliths in the inner Oisans–Pelvoux zone.

Figure S2. Backscattered electron images of mineral inclusions in Mn-rich garnet (Grt-1) of mafic HP granulite sample JB-19-43. Representative energy-dispersive X-Ray spectra of the different inclusions are shown below.

Figure S3. Complete set of mineral analyses for the samples from La Lavey, plotted on different diagrams. Colors and symbols correspond to different samples and textural settings respectively. The distribution of pixel composition obtained by processing of the quantitative X-Ray map (sample JB-19-56) on XmapTools is reported with blue contours. a) Ternary diagram with proportion of almandine+spessartine, pyrope and grossular end-members. b) Clinopyroxene analyses plotted on a Ca – Mg# diagram (Mg# = Mg/(Fe^{2+}+Mg)) and on a ternary showing the proportions of Augite, Jadeite and Aegyrine end-members. c) Al – Mg# composition of orthopyroxene. d) Amphibole analyses plotted on a Al(iv) –Mg#. The Ti distribution is added to the right. e) Proportion of anorthite in plagioclase. f) Ti –Mg# in biotite.

Figure S4. P-H_2O phase diagram computed with the composition of sample JB-19-43 (HP mafic granulite) and associated garnet isopleths. The bulk rock composition of this sample is very similar to that of the second HP mafic granulite JB-19-56, and hence variations are expected to be the same in the latter sample. According to this diagram, Ca-Mn-rich garnet can only grow at low P (<0.8 GPa) and for composition close to the fluid saturation.

Figure S5. Mineral proportions (in volume %) modeled with PerpleX for the P-T phase diagram computed with the bulk rock composition of sample JB-19-43.

Figure S6. Mineral proportions (in volume %) modeled with PerpleX, using the local X-Ray map composition of sample JB-19-56. The fit with observed proportion (indicated on the bottom right) has been assessed using the Q_{vol} criterion of Duesterhoeft and Lanari (2020). High Q_{vol} > 80% indicates good match between observations and the model.

Figure S7. Quantitative composition maps of amphibole, clinopyroxene and plagioclase in sample JB-19-56 processed with XmapTools.

Table S1. Settings and solution models used in PerpleX for phase equilibrium modeling

Table S2. Mineral EPMA data for the samples from La Lavey.

Table S3. Whole rock major and trace element compositions for the (retrogressed) mafic HP granulites

Table S4. Trace element analyses in rutile and Zr-in rutile temperatures computed using the calibration of Kohn (2020). T uncertainty is around ±20°C, which mainly arise from calibration uncertainty rather than uncertainty on Zr content. The detection limit for Zr is 25 ppm with the electron microprobe, and below 0.02 ppm with LA-ICPMS.

Table S5. Summary of trace element analyses in zircon, with Ti-in-zircon temperatures calculated with the calibration of Ferry and Watson (2007). Chondrite composition from Palme and O'Neill (2004).

Table S6. SIMS U-Pb analyses of zircon and LA-ICPMS U-Pb analyses of rutile in sample JB-19-56

Table S7. Compilation of metamorphic zircon and monazite U-Pb dates in the Oisans–Pelvoux massif. Data are from Fréville (2016) and this work.

FIGURES AND TABLES

Figure 1. Simplified geological map of the Paleozoic basement of the Oisans-Pelvoux, southern Belledonne and southern Grandes–Rousses Massifs in the external western Alps, redrawn from the BRGM 1:50 000 geological maps. Location of these domains in the Variscan Belt is shown in the bottom left insert. Zonation of the Variscan Belt modified from Ballèvre et al. (2014).

Figure 2. Geological map and cross-sections in the inner zone of the Oisans–Pelvoux massif, showing relationships between S2h (red) and S2v (black). The HP granulite formations of La Lavey are in yellow. Legends are the same as on Figure 1.

Figure 3. Field photographs of the investigated area and main lithologies. (a) – S2h flat-lying foliation in felsic migmatites, with sheared leucosomes marking top-to-the-South shearing. (b) – S2v steeply-dipping foliation in the sub-vertical migmatitic shear zones. Deformed amphibolite boudins mark a

sinistral kinematics. (c) – View on the granulitic formation of La Lavey, which consist in a hectometer-wide lens inserted in the flat-lying S2h. (d) – High-strain domain consisting of a mylonitic amphibole-plagioclase-rich layer alternating with retrogressed garnet-bearing granulites. (e) – Close up view of a massive, non-retrogressed garnet-clinopyroxene-bearing mafic HP granulite. (f) – Close-up view on a retrogressed mafic HP granulite from Peyre-Arguet.

Figure 4. Microscope photographs of the granulite samples. (a) – Large field view on the mineral assemblage in sample JB-19-56 (La Lavey). which shows the resorbed garnet and the destabilized clinopyroxene forming the relict HP assemblage. The coarse-grained HT assemblage composed of plagioclase+amphibole+biotite+orthopyroxene develops mainly around the resorbed garnet grains. (b) – Large garnet grain in sample JB-19-43, partly destabilized and surrounded by a kelyphite of plagioclase and amphibole. (c) – Alternating amphibole-rich and feldspar-rich layers in sample JB-19-55. Patches composed of a mosaic of fine-grained (<100 µm) euhedral to sub-euhedral clinopyroxene and plagioclase are preserved in the amphibole-rich layers, and interpreted as relics of the HT granulitic assemblage. (d) – Ilmenite rimed by titanite in sample JB-19-55. (e) – Mineral assemblage in retrogressed granulite sample JB-19-16. The matrix is mainly composed of plagioclase and amphibole with relict clinopyroxene, and garnet grains are partly resorbed and surrounded by a rim of plagioclase. Former symplectites have partly recrystalized into a mosaic assemblage of plagioclase + clinopyroxene ± amphibole. (f) – Mineral assemblage in garnet-free sample JB-19-18. Mineral abbreviation follow IUGS recommandation.

Figure 5. (a) – X-Ray map and composition profiles of garnet in samples JB-19-43 (a) and JB-19-56 (b), processed with XMapTools (Lanari et al., 2014). X-Ray maps in sample JB-19-56 were processed using the internal standardization approach of Lanari et al. (2018), and are therefore fully quantitative, while EDS map of sample JB-19-43 is only qualitative.

Figure 6. Quantitative X-Ray maps of clinopyroxene (a) and plagioclase (b) in sample JB-19-56, processed with XmapTools. The maps correspond to the same domain as in Figure 5-b). (c) – (d). Summary of clinopyroxene (c) and plagioclase (d) electron microprobe analyses in the three samples from La Lavey (JB-19-43, JB-19-55, JB-19-56). Composition of the re-integrated Na-rich

clinopyroxene in sample JB-19-56 is shown with a blue star. Distribution of pixel composition on the X-Ray map, obtained by processing with XMapTools, is represented with density contours.

Figure 7. Representative BSE images of rutile analyzed in different textural settings. (a) – (b) Rutile inclusions in garnet and matrix rutile in sample JB-19-43. Some rutile inclusions on image (a) display partial replacement by ilmenite; (c) – (d) primary rutile surrounded by titanite and secondary rutile growing over ilmenite in sample JB-19-55. (e) – Rutile inclusions in garnet of sample JB-19-16. (f) – Matrix rutile in sample JB-19-18.

Figure 8. Trace element composition of the (retrogressed) mafic granulites, normalized to the composition of N-MORB from Gale et al. (2013). E-MORB composition from Gale et al. (2013) is shown for comparison.

Figure 9. Phase diagrams computed with PerpleX and P–T constraints for the early prograde stage (a), the HP stage (b) and HT decompression (c). See description in text. The (+H2O) in phase diagram a) means that H_2O is treated as a saturated component, which is therefore stable in all fields.

Figure 10. (a) – Zr-Nb content in rutile measured *in-situ* by electron microprobe and on separated grains by LA-ICPMS. (b) – ZiR temperatures computed using the calibration of Kohn (2020), assuming P = 1.2 GPa (0.4 GPa for secondary rutile in sample JB-19-55). A typical uncertainty of ±20 °C is inferred combining analytical and calibration uncertainties.

Figure 11. (a) – Charge Contrast (CC) images of dated zircon grains and BSE images of representative rutile in sample JB-19-56, with reported positions of SIMS and LA-ICPMS spot analyses. (b) – REE profiles and trace element proxies used to identify the different zircon populations. Ti-in-zircon temperatures calculated using the calibration of Ferry and Watson (2007) are reported in the bottom right panel.

Figure 12. U-Pb zircon and rutile dating of sample JB-19-56. (a) – Zircon core analyses defining the age of the protolith; data uncorrected for common Pb. (b) – Tera-Wasserburg diagram of rutile U-Pb analyses, uncorrected for common Pb. (c) – Tera-Wasserburg diagram of zircon rim analyses

998 uncorrected for common Pb. The black arrow points to the $^{207}Pb/^{206}Pb$ value of present-day common Pb
999 according to Stacey and Kramers (1975). (d) – Kernel density estimate and histogram of $^{206}Pb/^{238}U$
1000 dates in zircon rims, corrected for common Pb according to the $^{207}Pb/^{206}Pb$ present-day value of the
1001 model of Stacey and Kramers (1975). Ellipses correspond to the 95% confidence interval of isotopic
1002 ratios.
1003
1004 Figure 13. Compilation of metamorphic zircon and monazite data from the Oisans–Pelvoux massif,
1005 taken from Fréville (2016) and this work. (a) Distribution of Variscan zircon and monazite $^{206}Pb/^{238}U$
1006 dates, obtained after filtering for the most discordant analyses (-5% < disc < 10 %, where discordance
1007 is expressed as the relative difference between the $^{206}Pb/^{238}U$ and the $^{207}Pb/^{235}U$ dates). Distinction
1008 between the intensely migmatized inner domain (East) and the Cortical domain (West) devoid of HT
1009 overprint is shown on Figure 1. (b) Plot of Th/U vs $^{206}Pb/^{238}U$ dates in zircon. Not all U-Pb zircon
1010 analyses plotted in (a) are shown here because they lack corresponding value for Th.
1011
1012 Figure 14 – Synthetic P-T-t evolution inferred for the mafic HP granulites from La Lavey (red path).
1013 Dotted lines indicate the two possible scenarios for decompression from stage 2 to stage 4 (see
1014 discussion in text). P–T path of retrogressed eclogites in northeast Belledonne (Jacob et al., 2021) is
1015 shown in blue for comparison.
1016
1017 Table 1. Localization and mineral composition of the investigated samples.

Sample	**JB-19-16**	**JB-19-18**	**JB-19-43**	**JB-19-55**	**JB-19-56**
Locality	Peyre-Arguet	Peyre-Arguet	La Lavey	La Lavey	La Lavey
Long °	6.35	6.35	6.22	6.22303	6.21990
Lat °	44.84	44.84	44.87	44.86517	44.86604
Alt (m)	2708	2674	2488	2731	2488
Rock type	Grt-bearing mafic granulite	Grt-free mafic granulite	Grt-bearing mafic granulite	Cpx-bearing amphibolite	Grt-bearing mafic granulite
Main minerals	Amp, Pl (sericitized), Grt, Qtz (+/-), Cpx (relics)	Amp, Cpx, Pl	Grt, Pl, Cpx, Opx, Amp, Bt, Qtz	Amp, Pl (sericitized), Cpx, rare Kfs	Grt, Pl, Cpx, Opx, Amp, Bt, Qtz
Accessory minerals	Ilm, Zrc, Rt (grt inclusions only)	Ilm, Zrc, rare Rt	Ilm, Rt (grt inclusions + matrix), Zrc	Ilm, Ttn (coronas arround Ilm), rare Rt	Ilm, Rt (grt inclusions only), Zrc

1018

Table 2. Summary of results of plagioclase-amphibole inverse thermometry (Holland and Blundy, 1994). For each sample, reported T is an average of results obtained on multiple plagioclase-amphibole pairs. Number of pairs (n) is given for each sample, and standard deviation is reported at 1σ. Temperatures were calculated directly from the X-Ray map with XMapTools for sample JB-19-56. Each pixel is treated as a single analysis, and therefore the reported number of pairs is very high.

Sample	Domain	n pairs	P GPa	T °C	±1σ (°C)
JB-19-56	granoblastic coronas (Na-rich Pl)	52600	1.2	763	25
JB-19-56	Symplectites (Na-rich Pl)	23400	1.2	764	27
JB-19-56	Garnet rim (Ca-rich Pl)	12340	0.8	833	35
JB-19-55	Amp-Pl layers (Pargasitic Hornblende)	13	0.4	656	34
JB-19-55	Amp-Pl layers (Actinolite)	3	0.4	573	44

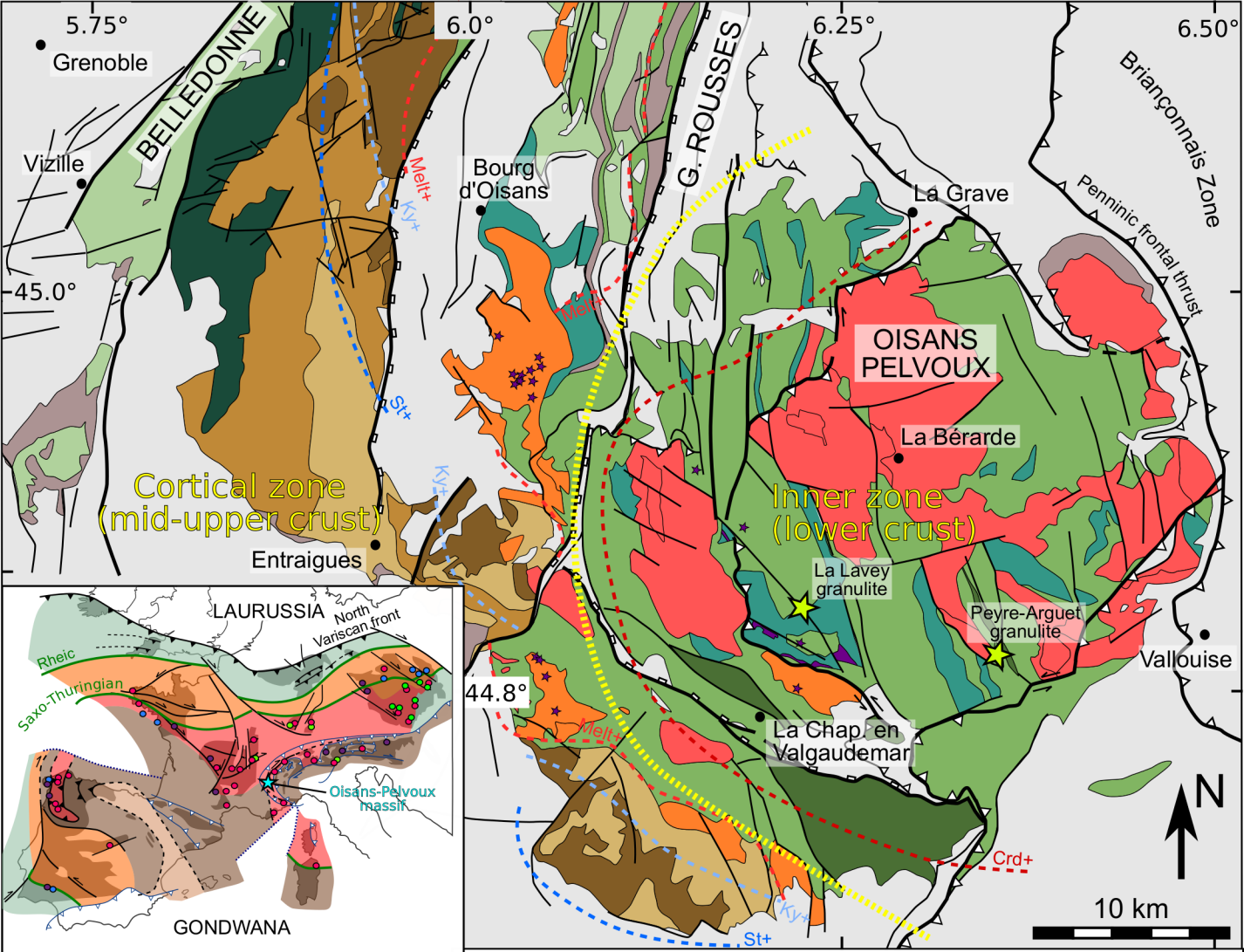
5.75°
6.0°
6.25°
6.50°
45.0°
44.8°
Grenoble
Vizille
Bourg d'Oisans
La Grave
Entraigues
Vallouise
La Bérarde
La Chapelle en Valgaudemar
BELLEDONNE
G. ROUSSES
Briançonnais Zone
Penninic frontal thrust
OISANS PELVOUX
Cortical zone (mid-upper crust)
Inner zone (lower crust)
La Lavey granulite
Peyre-Arguet granulite
Melt+
Ky+
St+
Crd+
N
10 km
LAURUSSIA
North Variscan front
Rheic
Saxo-Thuringian
Oisans-Pelvoux massif
GONDWANA
Exposed / covered
Rheno-hercynian zone
Oceanic suture
Ibero-Armorican / Saxo-Thuringian blocks
Oceanic suture
Moldanubian metamorphic allochtons
Parautochtonous, Gondwanan margin
Gondwanan foreland
Variscan sutures
Variscan thrusts /strike-slip faults
Alpine thrusts/ strike-slip faults
Variscan HP rocks
Blueschists
LT/HP eclogites
HT eclogites / HP granulites
Garnet peridotites
Cambrian-Ordovician series
Micaschist
Felsic gneiss and migmatite
Orthogneiss
Amphibolite
Mafic granulite
Ophiolitic complex: serpentinite, metagabbro, metabasalt (496 Ma)
Devonian-Tournaisian series
Micaschist, metaconglomerate
Volcanoclastic series
Magmatic complex: bimodal amphibolite-leptynite series (360-350 Ma)
Carbonifeous intrusive complex
Late Carboniferous granitoids (310-298-Ma)
Visean-Namurian granitoids (340–320 Ma)
High Mg – (ultra)-high K magmatism (plutons / enclaves and dykes)
Permian-Carboniferous deposits
Mesozoic cover
Crd+
Variscan metamorphic isograde
Mesozoic and Cenozoic faults

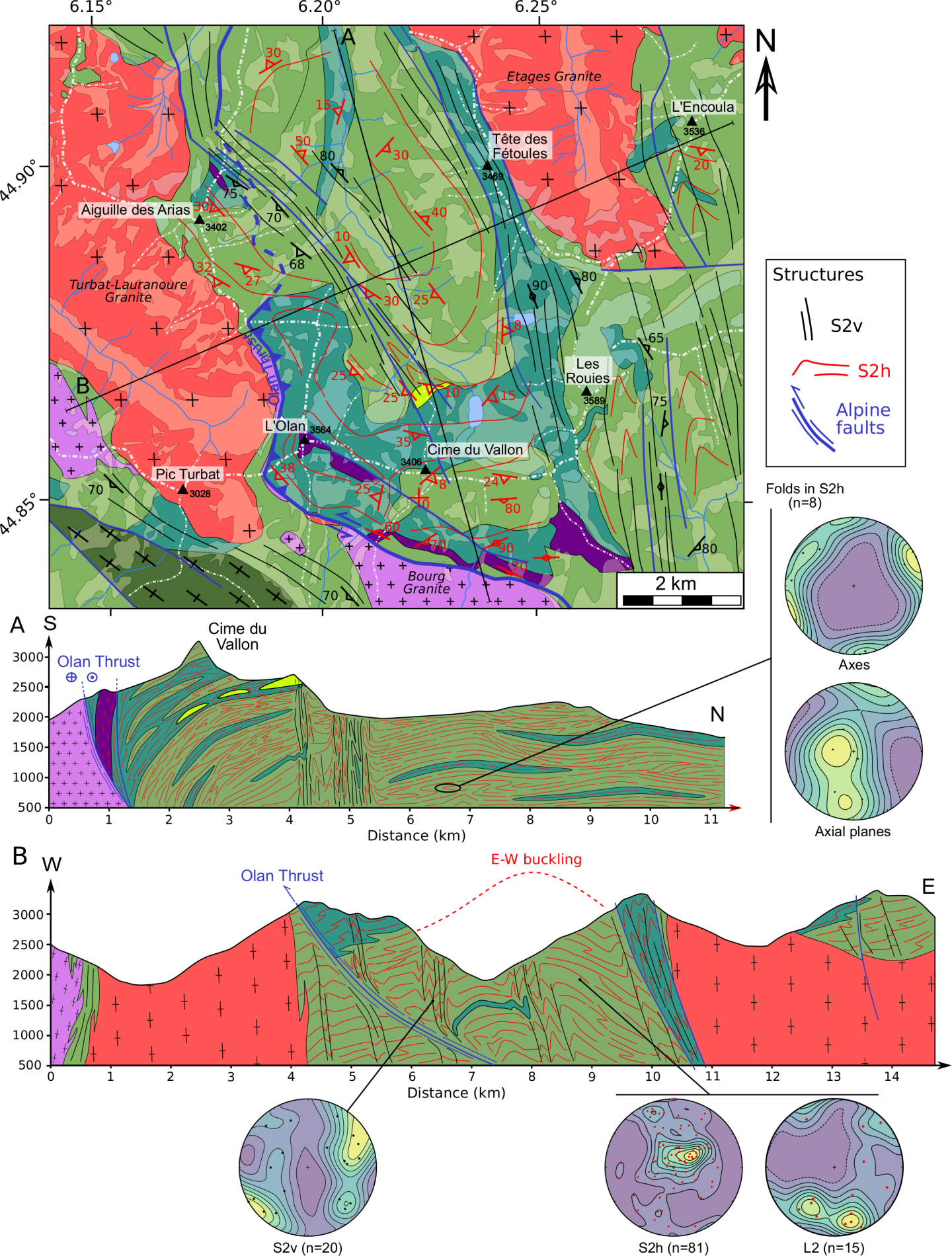
6.15°
6.20°
6.25°
44.90°
44.85°
A
B
N
Etages Granite
L'Encoula
3536
Tête des Fétoules
3489
Aiguille des Arias
3402
Turbat-Lauranoure Granite
Olan Thrust
L'Olan
3564
Les Rouies
3589
Cime du Vallon
3406
Pic Turbat
3028
Bourg Granite
2 km
Structures
S2v
S2h
Alpine faults
Folds in S2h (n=8)
Axes
Axial planes
A
S
N
Olan Thrust
Cime du Vallon
Distance (km)
B
W
E
Olan Thrust
E-W buckling
Distance (km)
S2v (n=20)
S2h (n=81)
L2 (n=15)

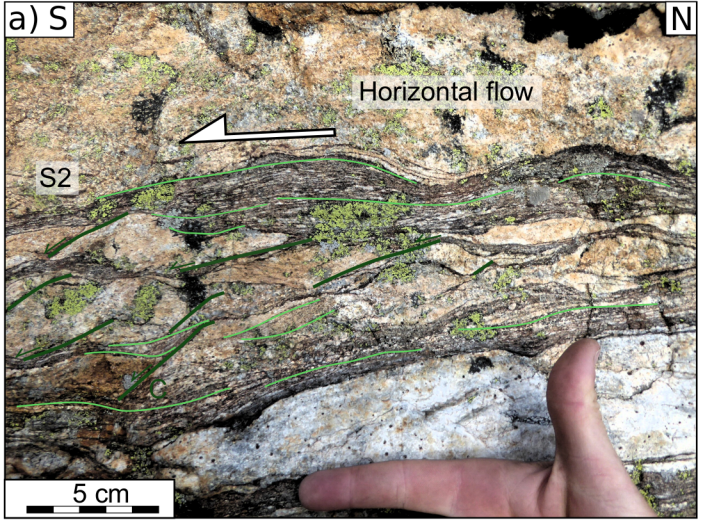
a) S
N
Horizontal flow
S2
5 cm

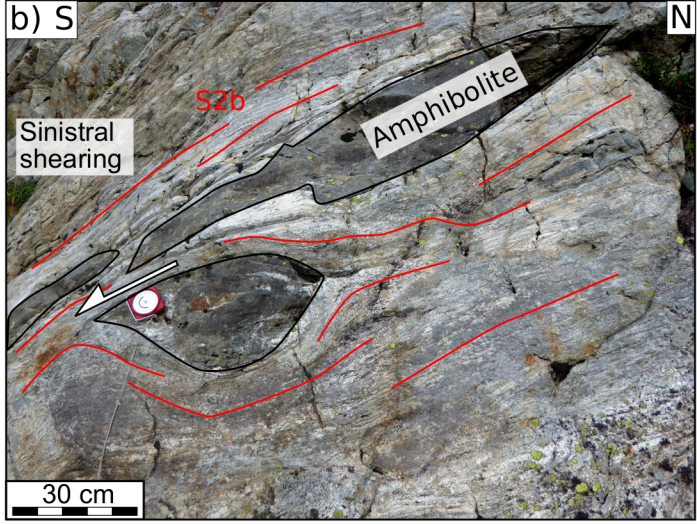
b) S
N
S2b
Amphibolite
Sinistral shearing
30 cm

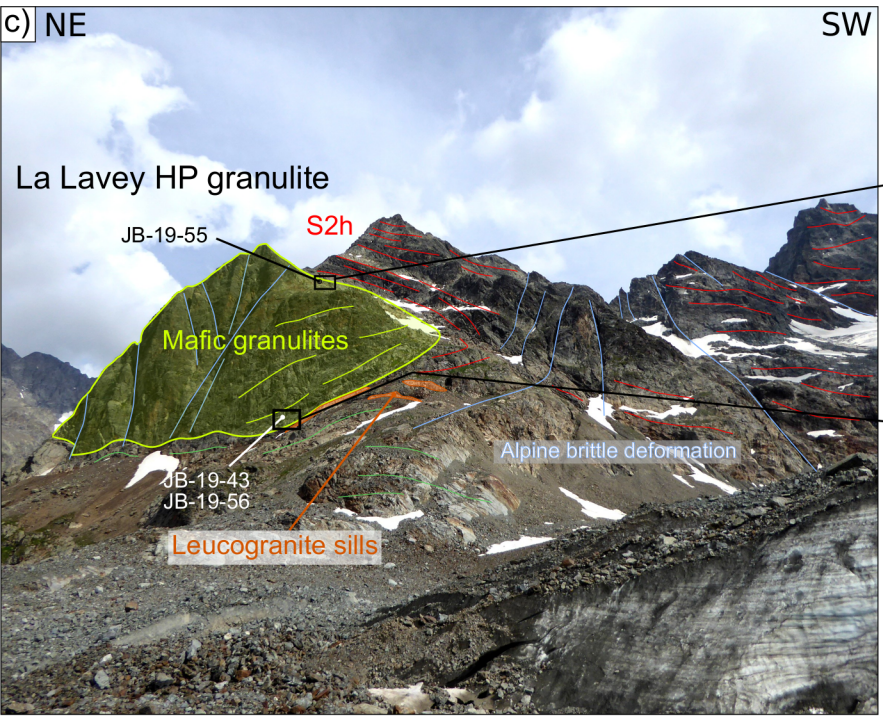
c) NE
SW
La Lavey HP granulite
JB-19-55
S2h
Mafic granulites
JB-19-43
JB-19-56
Leucogranite sills
Alpine brittle deformation

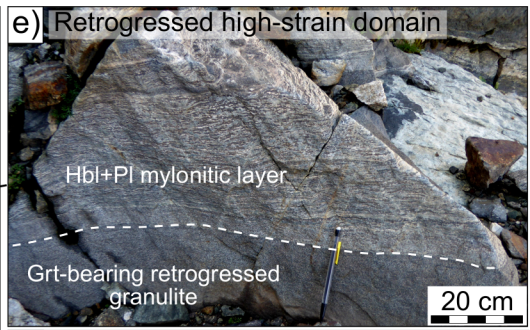
e) Retrogressed high-strain domain
Hbl+Pl mylonitic layer
Grt-bearing retrogressed granulite
20 cm

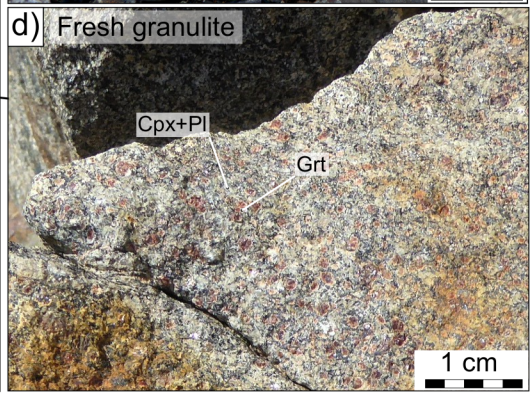
d) Fresh granulite
Cpx+Pl
Grt
1 cm

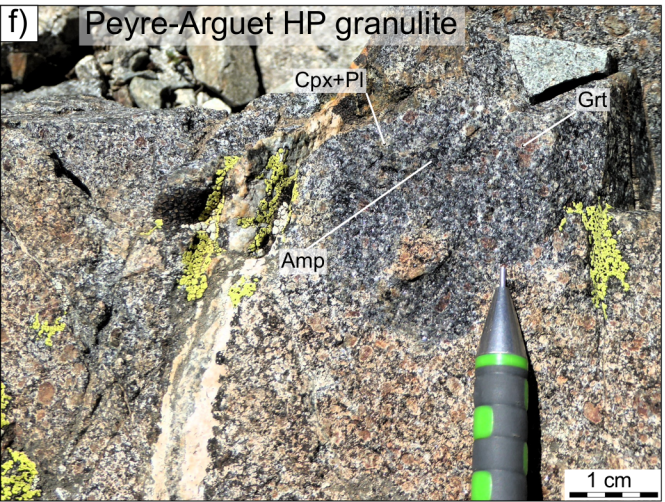
f) Peyre-Arguet HP granulite
Cpx+Pl
Grt
Amp
1 cm

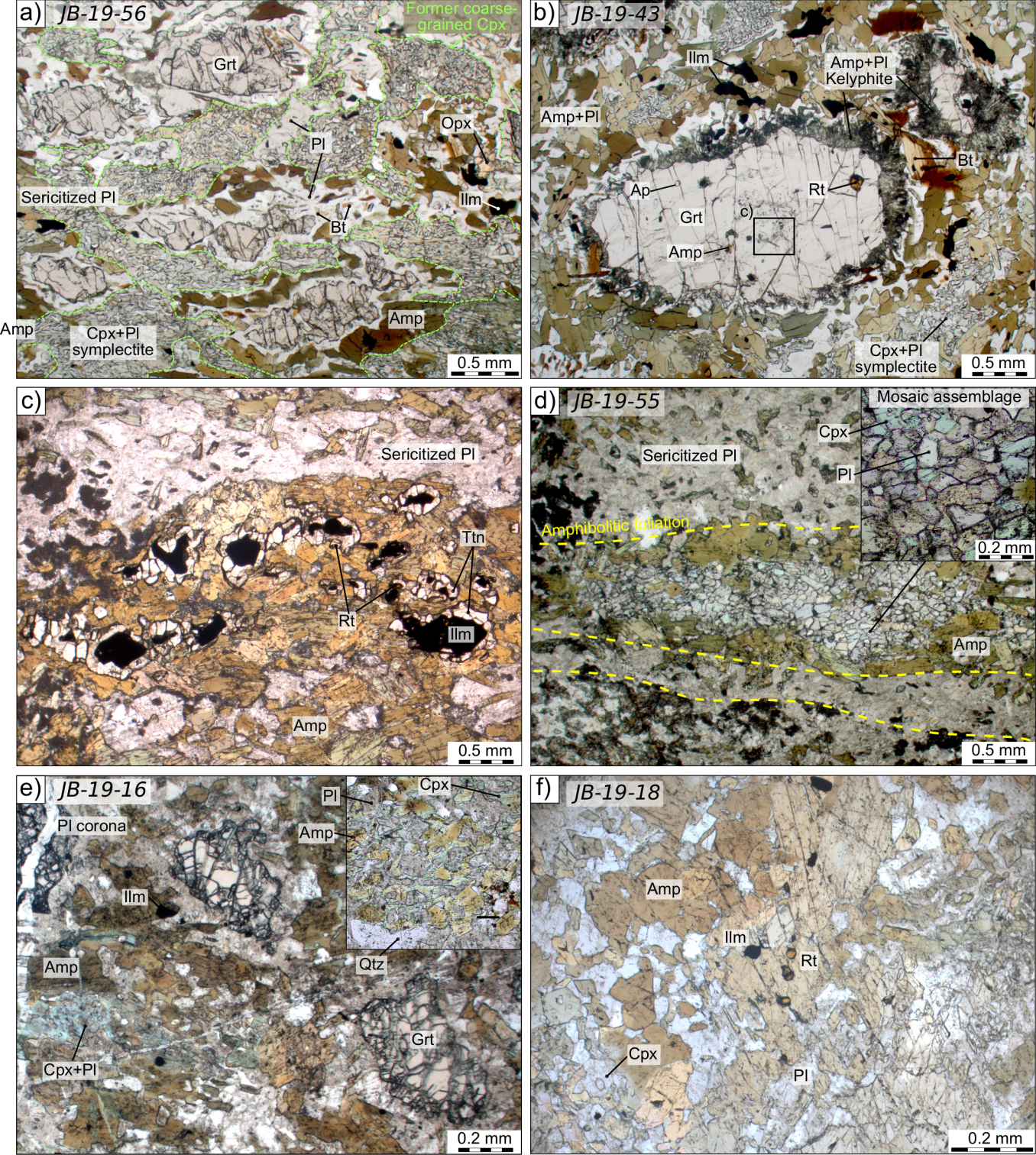
a)
JB-19-56
Former coarse-grained Cpx
Grt
Opx
Pl
Sericitized Pl
Ilm
Bt
Amp
Amp
Cpx+Pl symplectite
0.5 mm
b)
JB-19-43
Ilm
Amp+Pl Kelyphite
Amp+Pl
Bt
Ap
Rt
Grt
c)
Amp
Cpx+Pl symplectite
0.5 mm
c)
Sericitized Pl
Ttn
Rt
Ilm
Amp
0.5 mm
d)
JB-19-55
Mosaic assemblage
Cpx
Sericitized Pl
Pl
Amphibolitic foliation
0.2 mm
Amp
0.5 mm
e)
JB-19-16
Pl
Cpx
Pl corona
Amp
Ilm
Amp
Qtz
Grt
Cpx+Pl
0.2 mm
f)
JB-19-18
Amp
Ilm
Rt
Cpx
Pl
0.2 mm

a) Sample JB-19-43

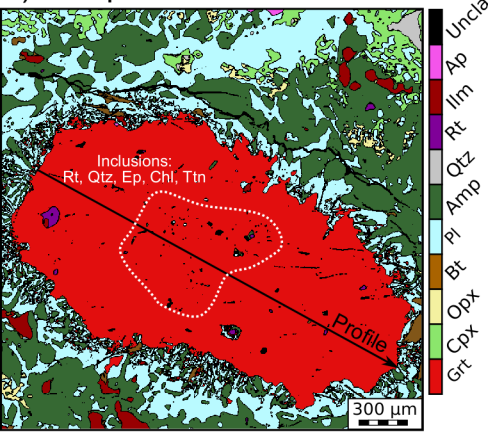

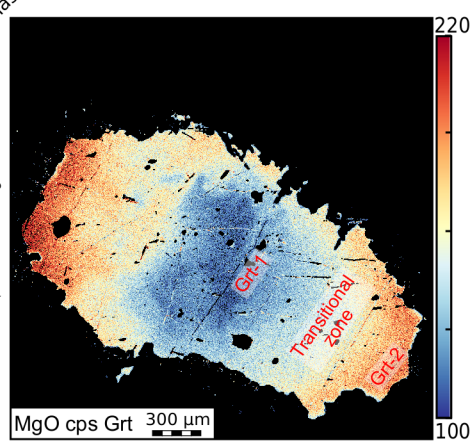

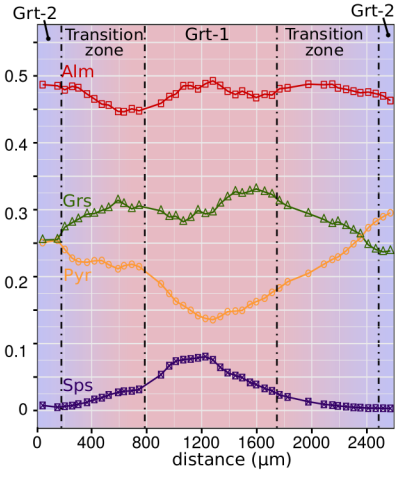

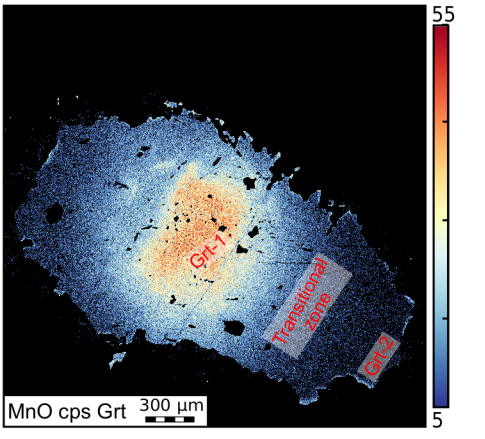

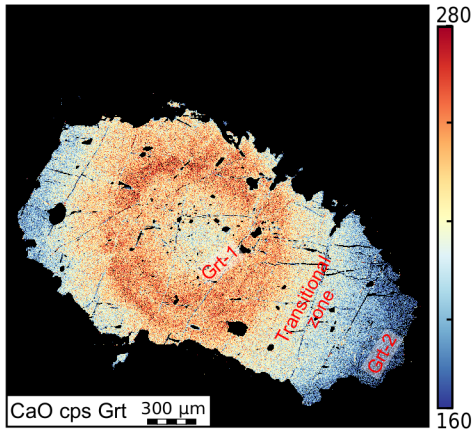

b) Sample JB-19-56

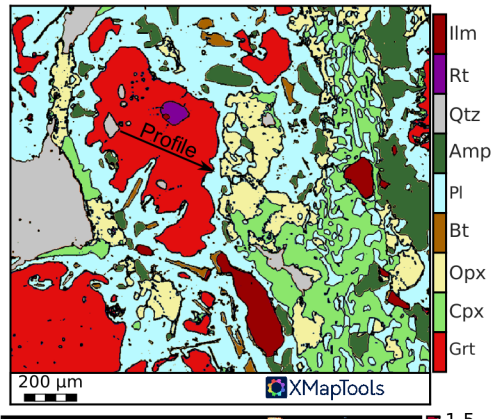

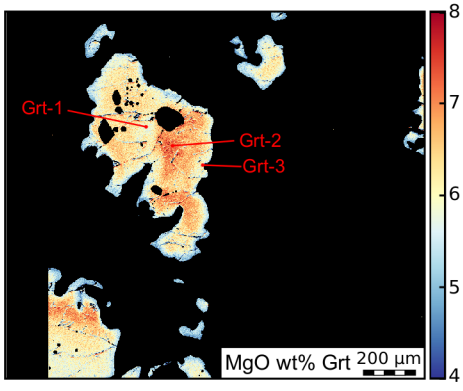

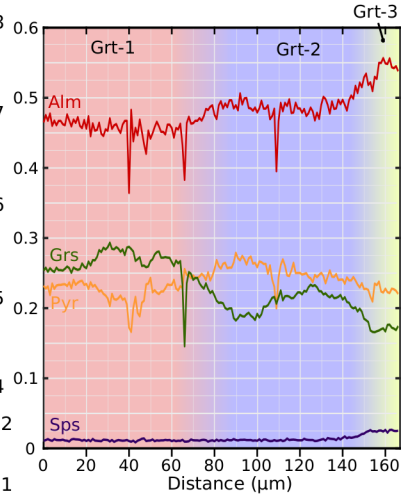

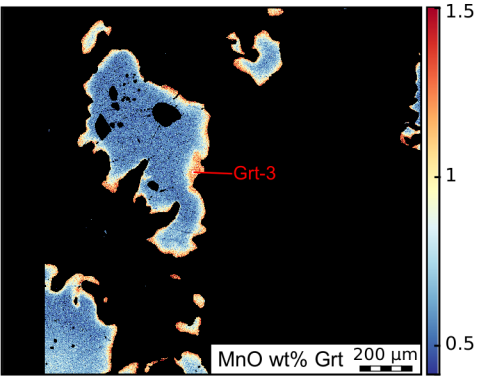

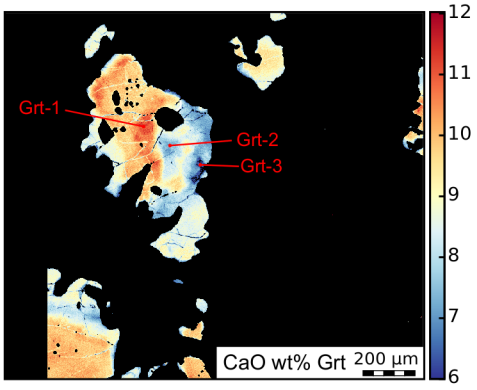

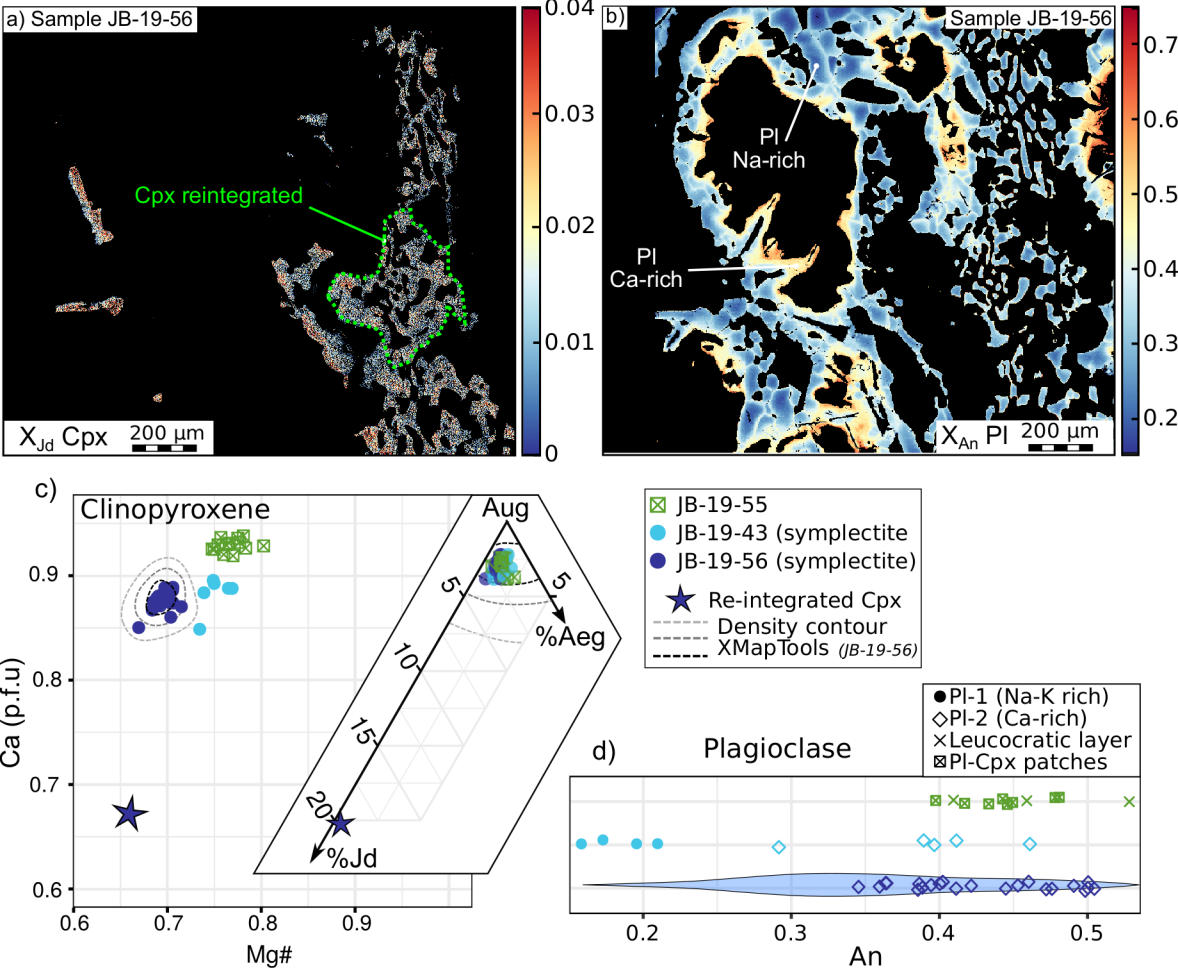
a) Sample JB-19-56
Cpx reintegrated
X_{Jd} Cpx
200 µm
0.04
0.03
0.02
0.01
0
b)
Sample JB-19-56
Pl
Na-rich
Pl
Ca-rich
X_{An} Pl
200 µm
0.7
0.6
0.5
0.4
0.3
0.2
c)
Clinopyroxene
Aug
%Aeg
%Jd
5
10
15
20
Ca (p.f.u)
Mg#
JB-19-55
JB-19-43 (symplectite
JB-19-56 (symplectite)
Re-integrated Cpx
Density contour
XMapTools (JB-19-56)
d)
Plagioclase
Pl-1 (Na-K rich)
Pl-2 (Ca-rich)
Leucocratic layer
Pl-Cpx patches
An

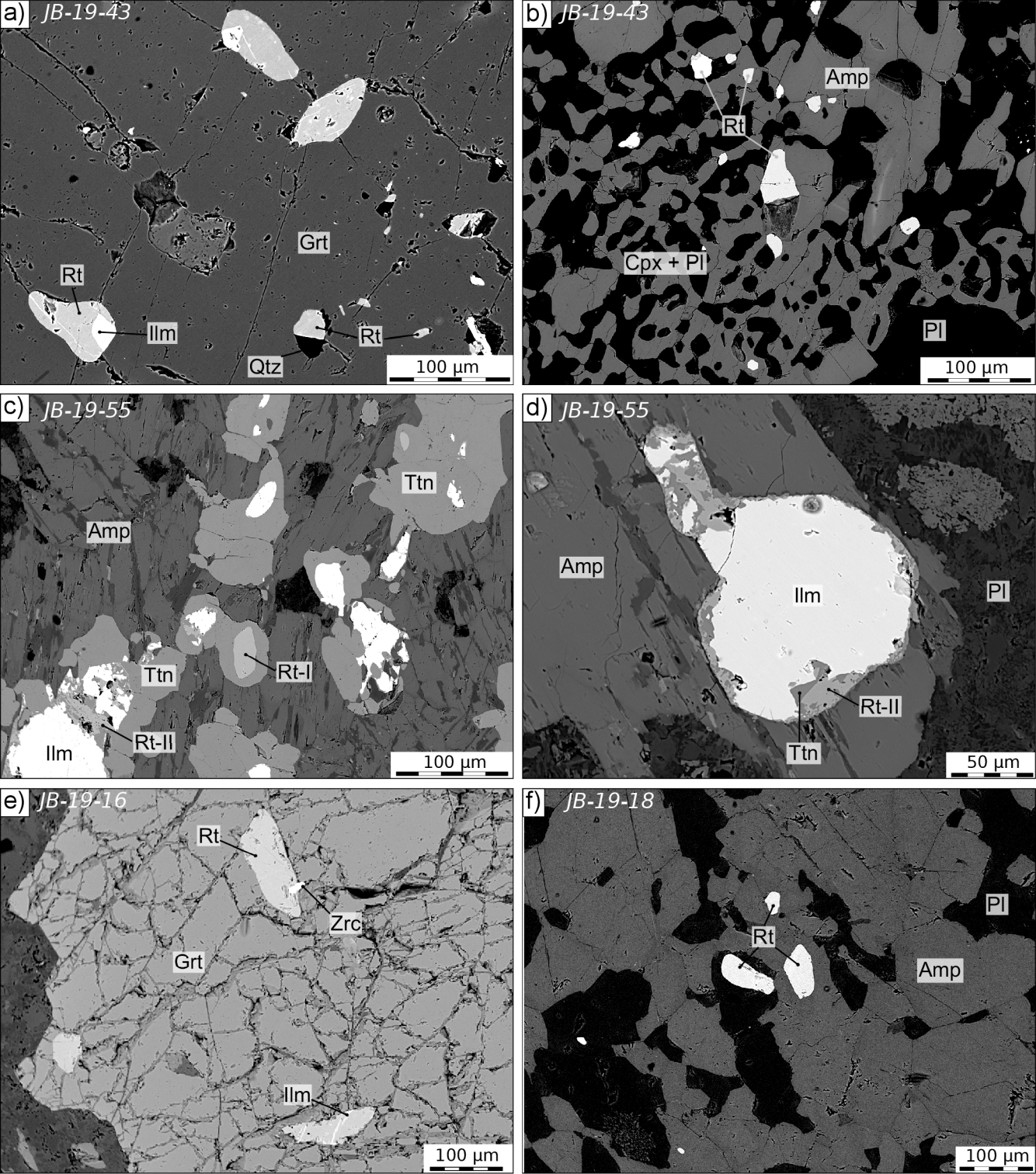
a)
JB-19-43
Grt
Rt
Ilm
Rt
Qtz
100 µm
b)
JB-19-43
Amp
Rt
Cpx + Pl
Pl
100 µm
c)
JB-19-55
Ttn
Amp
Ttn
Rt-I
Ilm
Rt-II
100 µm
d)
JB-19-55
Amp
Ilm
Pl
Rt-II
Ttn
50 µm
e)
JB-19-16
Rt
Zrc
Grt
Ilm
100 µm
f)
JB-19-18
Pl
Rt
Amp
100 µm

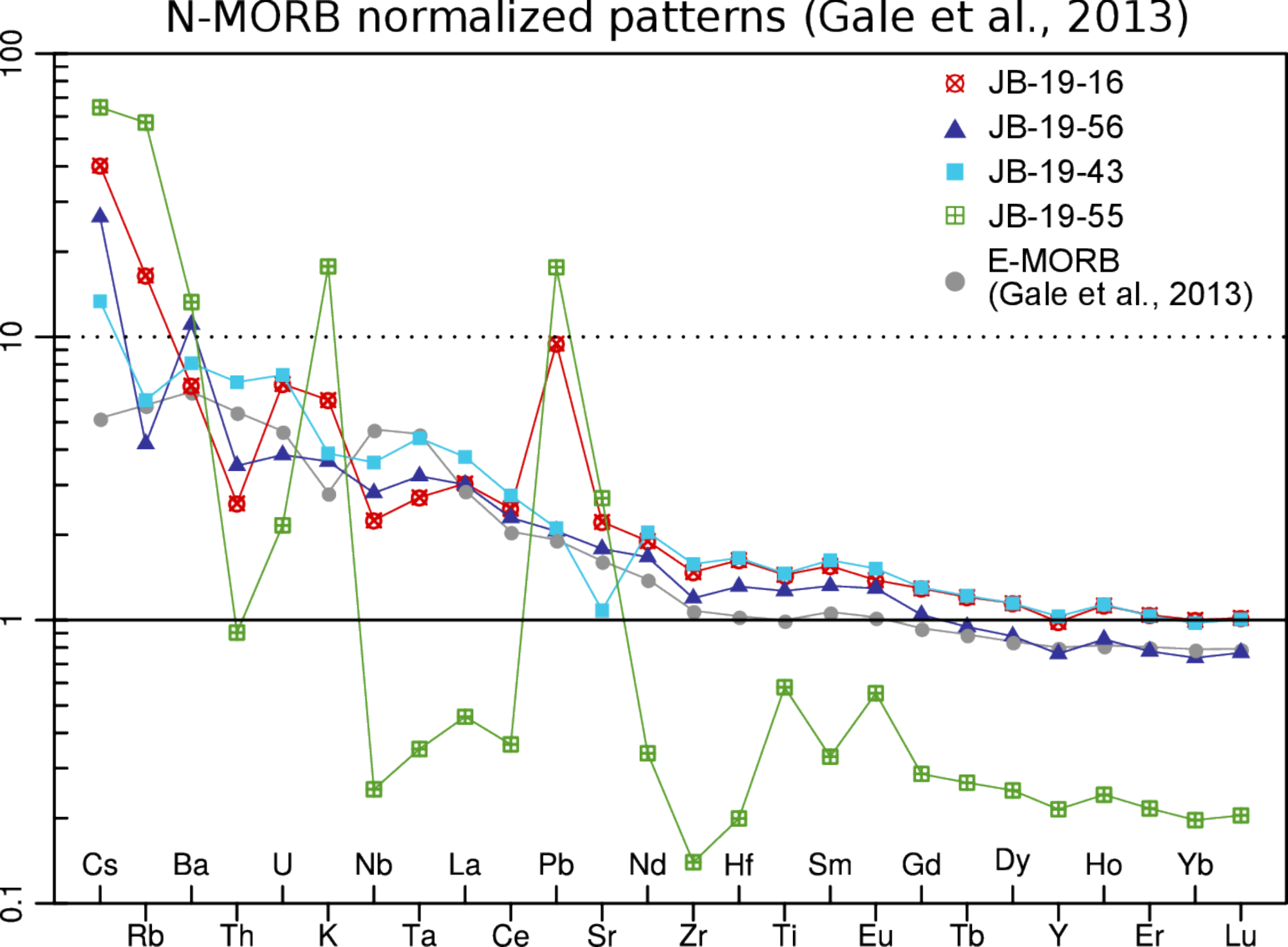
N-MORB normalized patterns (Gale et al., 2013)
100
10
1
0.1
JB-19-16
JB-19-56
JB-19-43
JB-19-55
E-MORB
(Gale et al., 2013)
Cs
Rb
Ba
Th
U
K
Nb
Ta
La
Ce
Pb
Sr
Nd
Zr
Hf
Ti
Sm
Eu
Gd
Tb
Dy
Y
Ho
Er
Yb
Lu

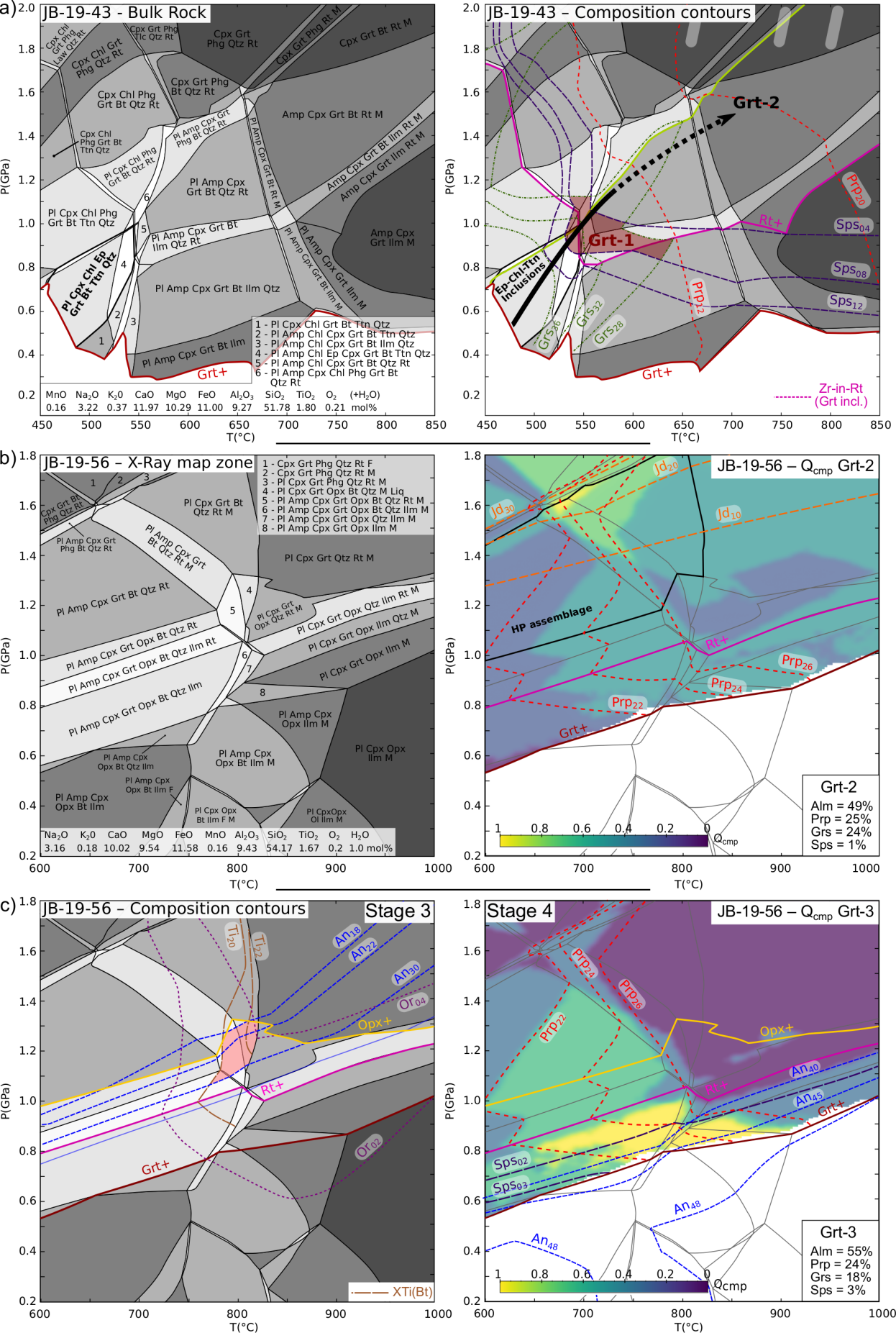
a)
JB-19-43 - Bulk Rock
JB-19-43 – Composition contours
Grt-1
Grt-2
Grt+
Rt+
Zr-in-Rt (Grt incl.)
Ep-Chl-Ttn inclusions
1 - Pl Cpx Chl Grt Bt Ttn Qtz
2 - Pl Amp Chl Cpx Grt Bt Ttn Qtz
3 - Pl Amp Chl Cpx Grt Bt Ilm Qtz
4 - Pl Amp Chl Ep Cpx Grt Bt Ttn Qtz
5 - Pl Amp Chl Cpx Grt Bt Qtz Rt
6 - Pl Amp Cpx Chl Phg Grt Bt Qtz Rt
MnO Na2O K2O CaO MgO FeO Al2O3 SiO2 TiO2 O2 (+H2O)
0.16 3.22 0.37 11.97 10.29 11.00 9.27 51.78 1.80 0.21 mol%
P(GPa)
T(°C)
b)
JB-19-56 – X-Ray map zone
1 - Cpx Grt Phg Qtz Rt F
2 - Cpx Grt Phg Qtz Rt M
3 - Pl Cpx Grt Phg Qtz Rt M
4 - Pl Cpx Grt Opx Bt Qtz M Liq
5 - Pl Amp Cpx Grt Opx Bt Qtz Rt M
6 - Pl Amp Cpx Grt Opx Bt Qtz Ilm M
7 - Pl Amp Cpx Grt Opx Qtz Ilm M
8 - Pl Amp Cpx Grt Opx Ilm M
Na2O K2O CaO MgO FeO MnO Al2O3 SiO2 TiO2 O2 H2O
3.16 0.18 10.02 9.54 11.58 0.16 9.43 54.17 1.67 0.2 1.0 mol%
JB-19-56 – Qcmp Grt-2
HP assemblage
Grt-2
Alm = 49%
Prp = 25%
Grs = 24%
Sps = 1%
Qcmp
c)
JB-19-56 – Composition contours
Stage 3
XTi(Bt)
Stage 4
JB-19-56 – Qcmp Grt-3
Grt-3
Alm = 55%
Prp = 24%
Grs = 18%
Sps = 3%

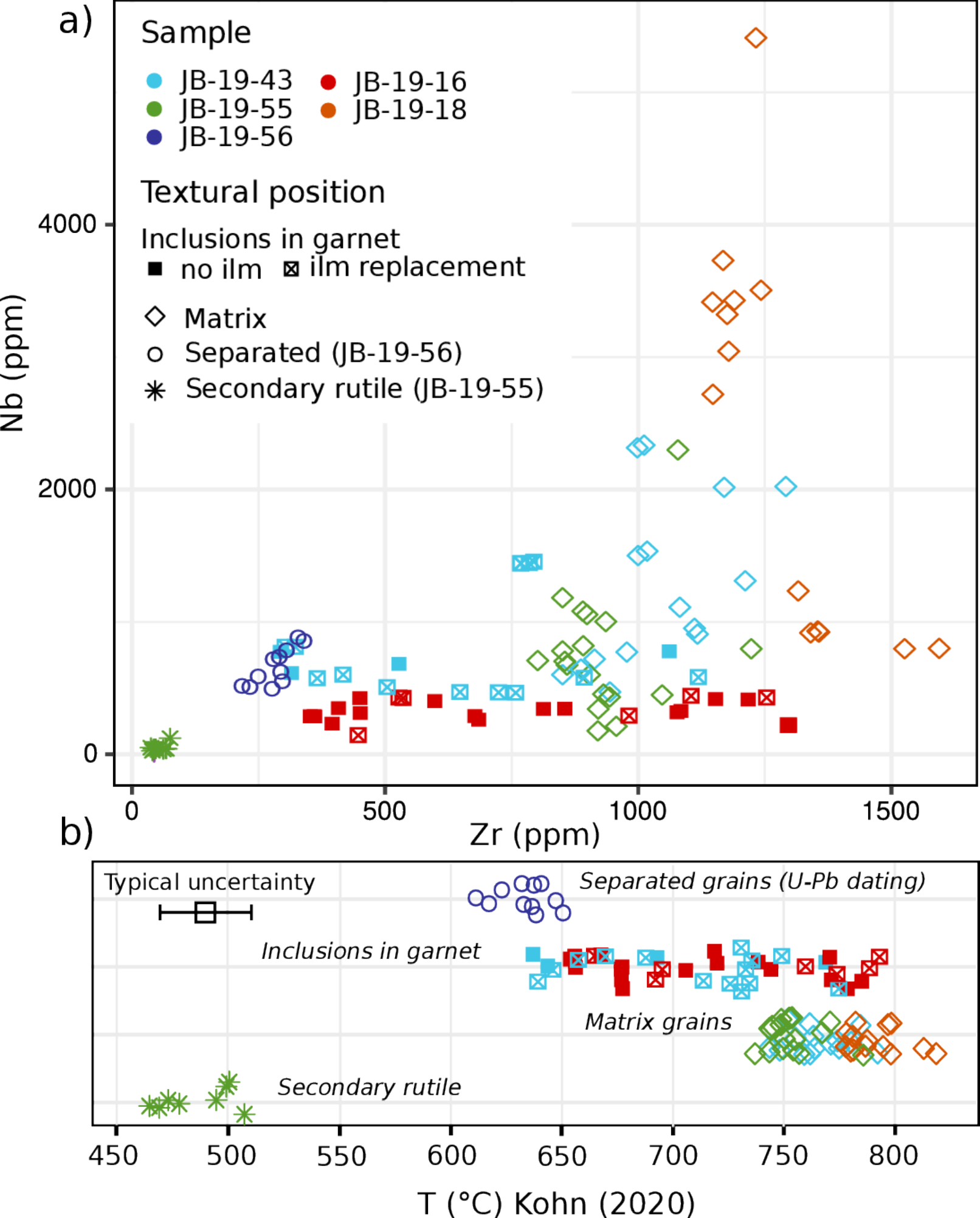
a)
Sample
JB-19-43
JB-19-16
JB-19-55
JB-19-18
JB-19-56
Textural position
Inclusions in garnet
no ilm
ilm replacement
Matrix
Separated (JB-19-56)
Secondary rutile (JB-19-55)
Nb (ppm)
4000
2000
0
0
500
1000
1500
Zr (ppm)
b)
Typical uncertainty
Separated grains (U-Pb dating)
Inclusions in garnet
Matrix grains
Secondary rutile
450
500
550
600
650
700
750
800
T (°C) Kohn (2020)

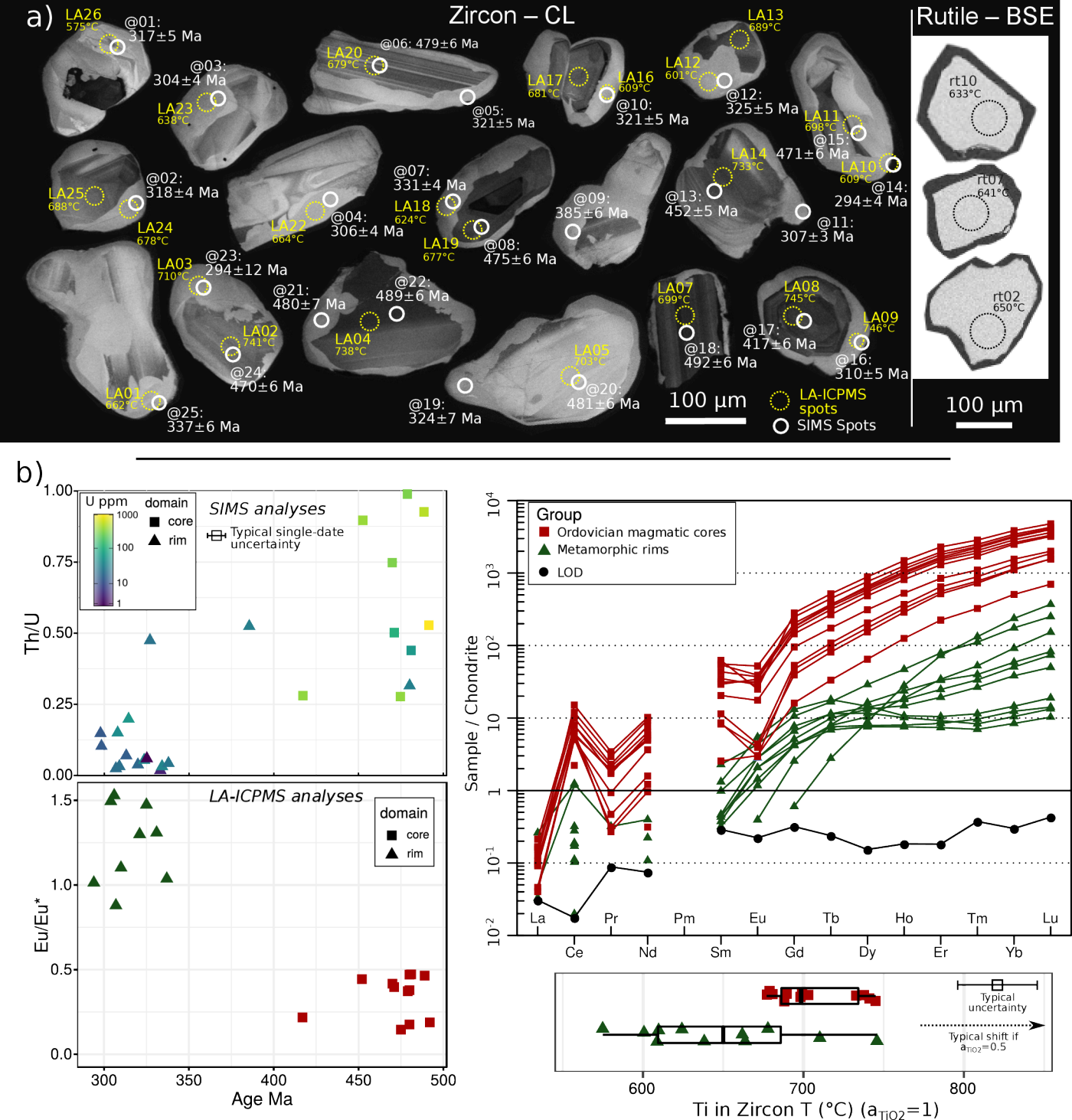
a)
Zircon – CL
Rutile – BSE
LA26 575°C
@01: 317±5 Ma
@03: 304±4 Ma
LA23 638°C
LA20 679°C
@06: 479±6 Ma
@05: 321±5 Ma
LA17 681°C
LA16 609°C
@10: 321±5 Ma
LA13 689°C
LA12 601°C
@12: 325±5 Ma
LA11 698°C
@15: 471±6 Ma
LA14 733°C
LA10 609°C
@14: 294±4 Ma
@13: 452±5 Ma
@11: 307±3 Ma
LA25 688°C
@02: 318±4 Ma
LA24 678°C
@07: 331±4 Ma
LA18 624°C
@09: 385±6 Ma
LA22 664°C
@04: 306±4 Ma
LA19 677°C
@08: 475±6 Ma
LA03 710°C
@23: 294±12 Ma
@21: 480±7 Ma
@22: 489±6 Ma
LA07 699°C
LA08 745°C
LA09 746°C
@17: 417±6 Ma
@18: 492±6 Ma
@16: 310±5 Ma
LA02 741°C
LA04 738°C
@24: 470±6 Ma
LA05 703°C
@20: 481±6 Ma
LA01 662°C
@25: 337±6 Ma
@19: 324±7 Ma
100 µm
LA-ICPMS spots
SIMS Spots
rt10 633°C
rt02 641°C
rt02 650°C
100 µm
b)
U ppm
1000
100
10
1
domain
core
rim
SIMS analyses
Typical single-date uncertainty
Th/U
1.00
0.75
0.50
0.25
0.00
LA-ICPMS analyses
domain
core
rim
Eu/Eu*
1.5
1.0
0.5
0.0
300
350
400
450
500
Age Ma
Group
Ordovician magmatic cores
Metamorphic rims
LOD
Sample / Chondrite
10^4
10^3
10^2
10
1
10^{-1}
10^{-2}
La
Ce
Pr
Nd
Pm
Sm
Eu
Gd
Tb
Dy
Ho
Er
Tm
Yb
Lu
Typical uncertainty
Typical shift if a_{TiO2}=0.5
600
700
800
Ti in Zircon T (°C) (a_{TiO2}=1)

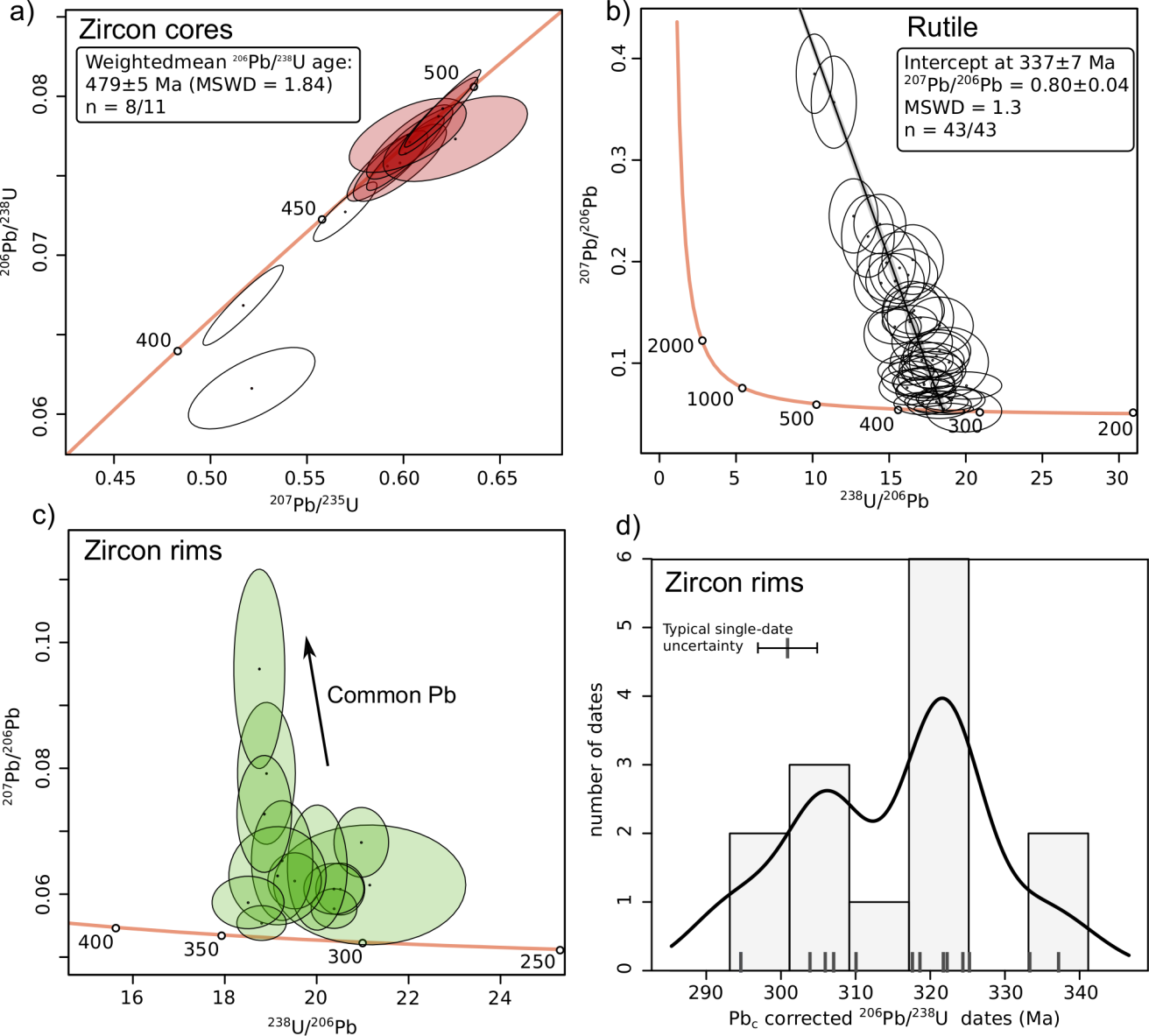
a)
Zircon cores
Weightedmean 206Pb/238U age:
479±5 Ma (MSWD = 1.84)
n = 8/11
500
450
400
206Pb/238U
207Pb/235U
b)
Rutile
Intercept at 337±7 Ma
207Pb/206Pb = 0.80±0.04
MSWD = 1.3
n = 43/43
2000
1000
500
400
300
200
207Pb/206Pb
238U/206Pb
c)
Zircon rims
Common Pb
400
350
300
250
207Pb/206Pb
238U/206Pb
d)
Zircon rims
Typical single-date
uncertainty
number of dates
Pbc corrected 206Pb/238U dates (Ma)

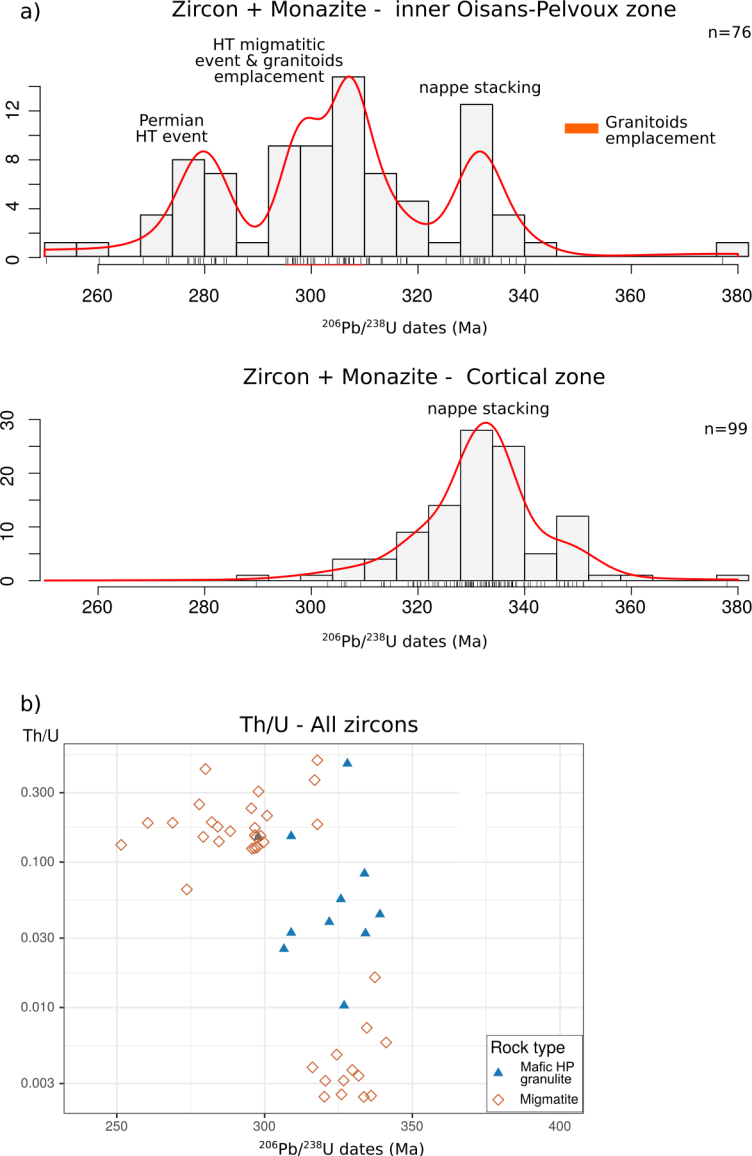
a)
Zircon + Monazite - inner Oisans-Pelvoux zone
n=76
HT migmatitic event & granitoids emplacement
nappe stacking
Permian HT event
Granitoids emplacement
0
4
8
12
260
280
300
320
340
360
380
206Pb/238U dates (Ma)
Zircon + Monazite - Cortical zone
nappe stacking
n=99
0
10
20
30
260
280
300
320
340
360
380
206Pb/238U dates (Ma)
b)
Th/U - All zircons
Th/U
0.300
0.100
0.030
0.010
0.003
250
300
350
400
206Pb/238U dates (Ma)
Rock type
Mafic HP granulite
Migmatite

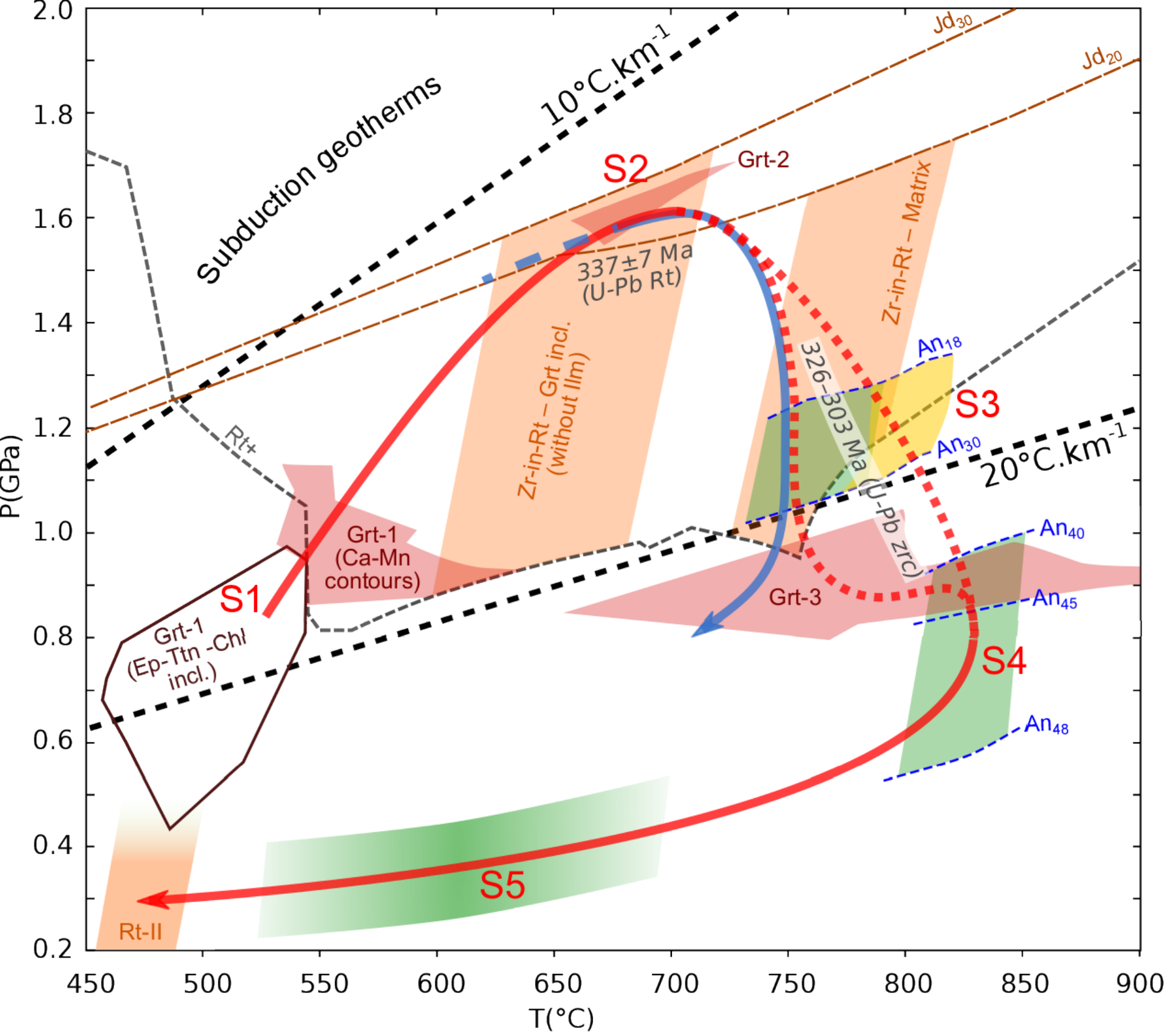
Subduction geotherms
10°C.km-1
20°C.km-1
Jd30
Jd20
S1
S2
S3
S4
S5
Grt-1 (Ep-Ttn -Chl incl.)
Grt-1 (Ca-Mn contours)
Grt-2
Grt-3
337±7 Ma (U-Pb Rt)
326–303 Ma (U-Pb zrc)
Zr-in-Rt – Grt incl. (without Ilm)
Zr-in-Rt – Matrix
An18
An30
An40
An45
An48
Rt+
Rt-II
P(GPa)
T(°C)
2.0
1.8
1.6
1.4
1.2
1.0
0.8
0.6
0.4
0.2
450
500
550
600
650
700
750
800
850
900
P-T paths
Inner Oisans–Pelvoux (this study)
NE Belledonne eclogites (Jacob et al., 2021)
Thermobarometric constrains
Garnet
Plagioclase-Amphibole (Holland and Blundy, 1994)
Zr-in-Rutile (Kohn, 2020)
Ti-in-Bt